The Astrophysical Journal, 807:171 (20pp), 2015 July 10 doi:10.1088/0004-637X/807/2/171

HIGH-RESOLUTION SPECTROSCOPIC STUDY OF EXTREMELY METAL-POOR STAR CANDIDATES FROM THE SKYMAPPER SURVEY*

Heather R. Jacobson[1], Stefan Keller[2], Anna Frebel[1], Andrew R. Casey[3,2], Martin Asplund[2], Michael S. Bessell[2], Gary S. Da Costa[2], Karin Lind[4], Anna F. Marino[2], John E. Norris[2], José M. Peña[1], Brian P. Schmidt[2], Patrick Tisserand[2], Jennifer M. Walsh[1,5], David Yong[2], and Qinsi Yu[1]
[1] Kavli Institute for Astrophysics and Space Research and Department of Physics, Massachusetts Institute of Technology, 77 Massachusetts Avenue, Cambridge, MA 02139, USA
[2] Research School of Astronomy & Astrophysics, The Australian National University, Cotter Road, Weston, ACT 2611, Australia
[3] Institute of Astronomy, University of Cambridge, Madingley Road, Cambridge CB3 0HA, UK
[4] Division of Astronomy and Space Physics, Department of Physics and Astronomy, Uppsala University, Box 516, SE-75120, Uppsala, Sweden
[5] Harvard University, Cambridge, MA 02138, USA
Received 2015 January 28; accepted 2015 March 25; published 2015 July 9

ABSTRACT

The SkyMapper Southern Sky Survey is carrying out a search for the most metal-poor stars in the Galaxy. It identifies candidates by way of its unique filter set which allows for estimation of stellar atmospheric parameters. The set includes a narrow filter centered on the Ca II K 3933 Å line, enabling a robust estimate of stellar metallicity. Promising candidates are then confirmed with spectroscopy. We present the analysis of Magellan Inamori Kyocera Echelle high-resolution spectroscopy of 122 metal-poor stars found by SkyMapper in the first two years of commissioning observations. Forty-one stars have [Fe/H] $\leqslant -3.0$. Nine have [Fe/H] $\leqslant -3.5$, with three at [Fe/H] ~ -4. A 1D LTE abundance analysis of the elements Li, C, Na, Mg, Al, Si, Ca, Sc, Ti, Cr, Mn, Co, Ni, Zn, Sr, Ba, and Eu shows these stars have [X/Fe] ratios typical of other halo stars. One star with low [X/Fe] values appears to be "Fe-enhanced," while another star has an extremely large [Sr/Ba] ratio: >2. Only one other star is known to have a comparable value. Seven stars are "CEMP-no" stars ([C/Fe] > 0.7, [Ba/Fe] < 0). 21 stars exhibit mild r-process element enhancements ($0.3 \leqslant$ [Eu/Fe] < 1.0), while four stars have [Eu/Fe] $\geqslant 1.0$. These results demonstrate the ability to identify extremely metal-poor stars from SkyMapper photometry, pointing to increased sample sizes and a better characterization of the metal-poor tail of the halo metallicity distribution function in the future.

Key words: stars: abundances

Supporting material: machine-readable tables

1. INTRODUCTION

The past few decades have seen many searches for the most chemically primitive, metal-poor stars in the Galaxy. Stars with [Fe/H][6] $\lesssim -3.0$ are very rare and much coveted because of the information they provide about conditions in the early universe. These stars are likely some of the first low-mass stars to form in the universe after the first chemical enrichment episodes occurred with the supernova deaths of metal-free Population III (Pop III) stars. Early theoretical work on the characterstics of Pop III stars indicated that they were short-lived, very massive ($\gtrsim 100\,M_{\odot}$) objects (Abel et al. 2002; Bromm & Larson 2004). More recent work has shown that the mass range of Pop III stars may have spanned ~3 orders of magnitude, leading to the possibility that some low-mass ($\sim 1 M_{\odot}$) stars may have survived to the present day (Hirano et al. 2014; Stacy & Bromm 2014; Susa et al. 2014). Independent of whether a relic Pop III star is ever found, the chemical compositions of the most metal-poor stars in the local universe provide a record of this first stellar generation.

The metallicity distribution function (MDF) of the most metal-poor stars in our Galaxy presents a history of the formation process of the Milky Way. It is a key constraint of any chemical evolution model that attempts to describe this process (e.g., Hartwick 1976). Early surveys for the most metal-poor stars in the halo (see below) indicated that the number of stars smoothly declined with metallicity (a factor of 10 in decline for every 1 dex in [Fe/H]) down to at least [Fe/H]~ −3.5. Lower than this, some samples indicated a sharp cut-off at [Fe/H] = −3.6, with very few stars more metal-poor than this value (Schörck et al. 2009; Li et al. 2010). However, this cut-off is not seen in other samples (Yong et al. 2013b). Searches for metal-poor stars in part have been driven to populate the most extreme metal-poor end of the MDF. We refer the reader to Frebel & Norris (2015) and references therein for an overview of the complexities involved in its interpretation.

Historically, surveys searched for extremely metal-poor (EMP) stars with [Fe/H] $\leqslant -3$ in the Galaxy halo. These surveys exploited the stars' tendency to have large proper motions (e.g., Ryan & Norris 1991; Carney et al. 1996) or the wide-field capabilities of Schmidt telescopes. Objective prism observations of millions of stars, carried out by such landmark surveys as the HK Survey (Beers et al. 1992) and the Hamburg-ESO Survey (Christlieb et al. 2008) on Schmidt telescopes led to the medium-resolution spectroscopic follow-up of thousands of EMP star candidates (Norris et al. 1999; Frebel et al. 2006; Schörck et al. 2009; Li et al. 2010; Placco et al. 2011). Of these, of order several hundred have been followed up with high-resolution spectroscopy and detailed

* This paper includes data gathered with the 6.5 m Magellan Telescopes located at Las Campanas Observatory, Chile.
[6] In the standard notation $[A/B] = \log_{10}(N_A/N_B) - \log_{10}(N_A/N_B)_{\odot}$, where N_A/N_B is the ratio of elements A and B by number, relative to that in the Sun ($\odot$).

element abundance analyses (e.g., McWilliam et al. 1995; Norris et al. 1996, 2013; Ryan et al. 1996; Aoki et al. 2002; François et al. 2003; Cayrel et al. 2004; Cohen et al. 2004, 2013; Lai et al. 2008; Hollek et al. 2011; Placco et al. 2014a; Roederer et al. 2014b).

More recently, medium-resolution spectroscopy of $\sim 10^5$ stars obtained by the Sloan Extension for Galactic Understanding and Exploration (SEGUE-I; Yanny et al. 2009) and SEGUE-II extensions of the Sloan Digital Sky Survey (York et al. 2000) have led to the identification of hundreds more EMP stars. Dozens of these have been observed with high resolution spectroscopy (e.g., Aoki et al. 2008, 2013a; Bonifacio et al. 2012; Caffau et al. 2013a, 2013b). A search for EMP stars is also underway with the Large-sky Area Multi-Object fiber Spectroscopic Telescope (LAMOST; Zhao et al. 2006; Cui et al. 2012), and high-resolution spectroscopic follow-up of the first candidates has recently been reported (Li et al. 2015).

EMP star candidate selection in objective prism surveys is based on the strength of the Ca II K line at 3933 Å in stellar spectra. This calcium line serves as a useful proxy for overall stellar metallicity. It is also possible to identify EMP candidates in pure photometric searches, but the determination of metallicity from broadband colors is difficult due their decreased sensitivity to metallicity at low [Fe/H] (however, see Schlaufman & Casey 2014). The SkyMapper Southern Sky Survey (Keller et al. 2007), being carried out with the SkyMapper 1.3 m telescope at Siding Spring Observatory in Australia, is a new survey that takes a rather hybrid approach. It combines the efficiency of an all-sky photometric survey with the power of metallicity measurements through narrow-band photometry of the Ca II K line, similar to what has been done in objective prism surveys.

SkyMapper's filter system is comprised of a *ugriz* set with the addition of a narrow Strömgren-like filter centered on the Ca II K line (Bessell et al. 2011). The combination of colors including this narrow filter provides constraints on stellar effective temperature, surface gravity, and metallicity. A "metallicity color index" therefore allows for the identification of metal-poor candidates from the photometry of the ~5 billion stars potentially observable by the survey. For more details about the survey techniques and candidate selection, see S. Keller et al. (2015, in preparation).

The most promising SkyMapper metal-poor candidates are selected for follow-up spectroscopic observation at both medium- and high-resolution. Three thousand one hundred ninety-eight candidates were selected from 5,452,735 stars in 195 SkyMapper fields. One thousand one hundred twenty-seven were followed up with medium-resolution spectroscopy and 259 with high-resolution spectroscopy. Indeed, one such candidate was verified as being the most Fe-poor star to date via medium- and high-resolution spectroscopic follow-up. The discovery and abundance pattern of SMSS J031300.36–670839.3, with [Fe/H] < -7.1, has already been reported (Keller et al. 2014). The addition of this star raises the number of stars known to have [Fe/H] $\leqslant -4.5$ to six (Christlieb et al. 2002; Frebel et al. 2005; Norris et al. 2007; Caffau et al. 2011; Hansen et al. 2014b; Keller et al. 2014), and the SkyMapper EMP star candidate selection technique shows the promise of finding more of these stars. A corresponding survey for the most metal-poor and oldest stars in the Galactic bulge using SkyMapper photometry and AAOmega/AAT multi-object spectroscopy is also underway (PI M. Asplund; see Howes et al. 2014 for first results).

In this work, we present results of the high-resolution spectroscopic follow-up of other metal-poor star candidates identified by SkyMapper from 2011 to 2013 November. As described in S. Keller et al. (2015, in preparation), the SkyMapper photometry used to select these candidates was obtained during the commissioning phase of the survey. Section 2 describes the target selection, observations, and data, and Section 3 describes our method of analysis. Results are presented in Section 4, while a discussion and summary are given in Sections 5 and 6.

2. TARGET SELECTION, OBSERVATIONS AND DATA REDUCTION

Most of the candidate metal-poor stars were first observed with the Wide Field Spectrograph on the ANU 2.3 m telescope, providing medium-resolution ($R \sim 3000$) optical spectra. Stellar parameters and metallicities were estimated based on a comparison of the spectra to a library of synthetic spectra (S. Keller et al. 2015, in preparation). However, for some early Magellan observing runs (2012 February, 2012 May), candidates were selected based on metallicity estimates from their SkyMapper photometry alone. At that time, the color–metallicity calibration of the SkyMapper filter set was still being developed and improved, so a number of the candidates turned out to be metal-rich. A preliminary analysis of 160 stars from these early campaigns found 46 stars to have [Fe/H] $\geqslant -1$, 85 stars with $-2 \leqslant$[Fe/H] < -1 and 29 stars to have [Fe/H] < -2. We have therefore made a metallicity cut and here are presenting the results for only 24 stars with [Fe/H] $\lesssim -2.2$ as measured from high-resolution spectra. For the later observing runs (2012 September forward), all candidates were selected from medium-resolution spectroscopy, and we analyzed all stars observed in these runs including the metal-rich ones. (Ten stars have [Fe/H] > -2.2.) Nine candidates were selected based on preliminary photometry that did not pass subsequent quality cuts. As such, these objects do not have SMSS photometry or coordinates and instead we have adopted 2MASS identifiers and coordinates (Skrutskie et al. 2006).

The spectra analyzed in this work were obtained with the Magellan Inamori Kyocera Echelle (MIKE) spectrograph on the 6.5 m Magellan Clay Telescope at Las Campanas Observatory (Bernstein et al. 2003). Observations spanned multiple campaigns from 2011 to 2013 November. Depending on sky conditions, spectra were obtained with either the 0.″7 or 1.″0 slits, resulting in spectral resolutions ($R \equiv \lambda/\Delta\lambda$) of $R \sim 35{,}000$ in the blue and $R \sim 28{,}000$ in the red, and $R \sim 28{,}000$ in the blue and R~22,000 in the red, for the smaller and larger slit sizes, respectively. Exposure times generally ranged from 300 to 1800 s, depending on the brightness of the target, to obtain "snapshot" spectra with which to confirm EMP star candidates. For some of the fainter, more promising targets, multiple (2–4) exposures were obtained to increase the signal-to-noise ratios (S/Ns). All spectra span nearly the full optical range, 3350–9000 Å, but the S/N was generally too low blueward of ~3800 Å for analysis. Details of the observations are given in Table 1, including star ID number, J2000 coordinates, g magnitude, and g–i color from the SkyMapper observations (see S. Keller et al. 2015, in preparation for details of the SkyMapper photometric system). Also included are the UT date, the total exposure time in seconds, the slit size used, the measured radial velocity (see the next Section), and the S/N (per pixel) measured at 4500 and

Table 1
Observing Details

Star	α (J2000)	δ (J2000)	g mag	$g-i$ mag	UT date[a]	t_{exp} (s)	Slit size (arcsec)	v_{rad} (km s^{-1})	S/N pixel^{-1} 4500 Å	S/N pixel^{-1} 6000 Å
SMSS J000113.96–363337.9	00 01 13.96	−36 33 37.9	14.375	1.014	2013 Jan 08	1200	0.7	243.3	49	51
SMSS J001039.86–525851.4	00 10 39.86	−52 58 51.4	14.628	1.137	2013 Jan 08	1500	0.7	110.0	32	64
SMSS J001952.15–525803.0	00 19 52.15	−52 58 03.0	15.378	1.176	2013 Jan 07	2720	0.7	154.8	28	52
SMSS J002148.06–471132.1	00 21 48.06	−47 11 32.1	15.072	0.932	2013 Jan 07	1200	0.7	204.5	20	33
SMSS J003055.81–482011.3	00 30 55.81	−48 20 11.3	13.980	1.119	2013 Jan 08	900	0.7	109.3	38	63
SMSS J003327.36–491037.9	00 33 27.36	−49 10 37.9	15.656	0.974	2013 Jan 07	2400	0.7	84.7	40	49
SMSS J004037.56–515025.2	00 40 37.56	−51 50 25.2	14.617	0.939	2013 Jan 07	2700	0.7	72.9	19	33
SMSS J005953.98–594329.9	00 59 53.98	−59 43 29.9	14.925	0.381	2013 Nov 17	10140	0.7	376.7	78	105
SMSS J010332.63–534654.3	01 03 32.63	−53 46 54.3	14.689	0.847	2013 Jan 08	1200	1.0	96.6	51	50
SMSS J010651.91–524410.5	01 06 51.91	−52 44 10.5	14.134	1.025	2013 Jan 06	1800	1.0	189.5	67	83

Notes.
[a] UT at start of observation.
[b] Suspected binary.

(This table is available in its entirety in machine-readable form.)

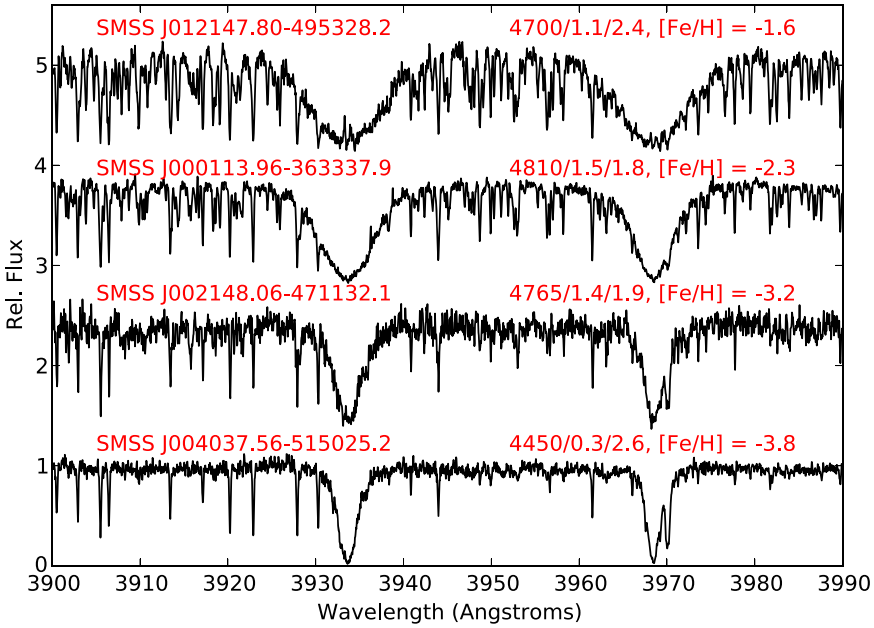

Figure 1. Portions of the MIKE spectra for four stars in our sample around the Ca II H and K lines. LTE stellar parameters and metallicities determined in our analysis are also indicated ("T_{eff}/log g/v_t, [Fe/H]"). Note the variations in line strength with decreasing [Fe/H] (top to bottom).

6000 Å. The average($\pm 1\sigma$) S/Ns of the sample are 35($\pm$15) and 55($\pm$21) at 4500 and 6000 Å, respectively.

All spectra were reduced using the CarPy data reduction pipeline[7] described in Kelson (2003). Individual exposures were combined to increase S/N, individual orders were merged, and the blue and red spectra were combined and then continuum normalized to create one continuous spectrum per star.

Example MIKE spectra for four stars are presented in Figure 1, all obtained with the 0.″7 slit. Their stellar parameters and metallicities, as determined in our analysis, are also indicated. All told, the total sample of analyzed stars is 122. For candidates selected based on metallicity estimates from medium-resolution spectroscopy, agreement between $[Fe/H]_{MRS}$ and $[Fe/H]_{HRS}$ measured in this work generally agrees at the 0.3 dex level (S. Keller et al. 2015, in preparation).

3. ANALYSIS

Our abundance analysis software (Casey 2014) incorporates the Castelli & Kurucz 1D LTE hydrostatic model atmosphere grid (Castelli & Kurucz 2004) and the version of the LTE abundance analysis program MOOG that includes treatment of Rayleigh scattering (Sneden 1973; Sobeck et al. 2011). Our line list was that compiled by Roederer et al. (2010b), though we only considered lines within the wavelength range 3500–6500 Å.

Radial velocities for our stars were determined via cross-correlation of the Ca triplet (λ8450–8700) and/or Mg Ib (λ5150–5200) region of the spectra against that of a high S/N, restframe MIKE spectrum of the metal-poor standard star HD 140283. Velocity errors due to the cross-correlation

[7] See http://code.obs.carnegiescience.edu/mike.

Table 2
Stellar Parameters

Star	$T_{\rm eff}$ (K)	log(*g*) LTE (dex)	[Fe/H] LTE (dex)	$v_{\rm micr}$ (km s^{-1})	log(*g*) NLTE (dex)	[Fe/H] NLTE (dex)
SMSS J000113.96–363337.9	4810	1.60	−2.32	1.80	1.90	−2.21
SMSS J001039.86–525851.4	4711	1.20	−2.32	2.20	1.56	−2.18
SMSS J001952.15–525803.0	4639	1.20	−2.56	2.40	1.56	−2.43
SMSS J002148.06–471132.1	4765	1.40	−3.17	2.10	1.90	−3.00
SMSS J003055.81–482011.3	4720	1.50	−2.53	2.50	1.82	−2.41
SMSS J003327.36–491037.9	4630	0.80	−3.36	2.35	1.37	−3.17
SMSS J004037.56–515025.2	4468	0.55	−3.83	2.45	1.05	−3.67
SMSS J005953.98–594329.9	5413	2.95	−3.94	1.40	3.41	−3.78
SMSS J010332.63–534654.3	4810	1.40	−3.03	1.80	1.90	−2.86
SMSS J010651.91–524410.5	4486	0.65	−3.79	2.60	1.15	−3.63

(This table is available in its entirety in machine-readable form.)

technique are generally small (0.1–0.3 km s^{-1}). Based on repeat observations of standard stars such as HD 122563, G64–12, and HD 13979 during each observing run, we estimate a zero-point offset to our radial velocity scale of 1–2 km s^{-1}, with our values being smaller than ones in the literature for these stars.

Four stars were observed in two separate observing runs, and two stars were observed in three different campaigns. The radial velocities determined from the different spectra of these stars also show differences of 1–2 km s^{-1}, with the exception of the star SMSS J022410.38–534659.9, which shows a variation of ∼14 km s^{-1}. This star may be a single-lined spectroscopic binary, however, its stellar parameters (see next Section) place it on the edge of the instability strip in the Hertzsprung–Russell diagram, so it may instead be a variable. For those stars observed with the same slit size in multiple observing runs, all the spectra were combined to increase S/N before the abundance analysis. For those stars observed with different slit sizes, the spectrum with the highest S/N was analyzed; in cases where S/N levels were comparable, the 0.″7 spectrum was analyzed.[8]

Heliocentric radial velocities for each of the stars are given in Table 1. As can be seen, many have large heliocentric velocities as expected for halo stars. All spectra were shifted to rest wavelength for the abundance analysis described in the next section.

3.1. Determination of Stellar Parameters

The stellar parameters for each star were determined solely from its MIKE spectrum using the standard spectroscopic techniques: effective temperature ($T_{\rm eff}$) by removal of any slope of Fe I abundance with excitation potential (E.P.), log *g* by matching Fe I and Fe II abundances, microturbulence (v_t) by removal of any slope of Fe I abundance with reduced equivalent width. In this process, individual lines with abundances ∼2σ away from the mean were visually inspected, reassessed for measurement quality, and if necessary, rejected (due to blending, uncertainty in continuum placement, etc.). Our general tolerances were as follows: slope of log ϵ(Fe I) versus E.P. < 0.005 dex eV^{-1}, [Fe II/H] − [Fe I/H] < 0.05 dex, and slope of log ϵ(Fe I) versus log(RW) < 0.005. The [M/H] of the model atmosphere was set to [Fe I/H]+0.25 as described in Frebel et al. (2013).

Spectroscopic effective temperatures are generally cooler than photometric temperatures due to departures from local thermodynamic equilibrium (LTE; Johnson 2002; Cayrel et al. 2004; Lai et al. 2008; Hollek et al. 2011; Lind et al. 2012; Cohen et al. 2013). The use of 1D models as opposed to time-dependent 3D or temporally and spatially averaged 3D (⟨3D⟩) models can also lead to this effect (Asplund 2005; Bergemann et al. 2012b). Too-cool temperatures translate into smaller log *g* and larger v_t values than would be found using photometric temperatures. We have adopted the effective temperature correction presented in Frebel et al. (2013). It places spectroscopically determined temperatures on a scale similar to that found by photometric temperature methods. This correction is appropriate for the program stars, and the majority of them span the metallicity range for which the correction has been tested (−3.3 < [Fe/H] < −2.5).[9] The final adopted (corrected) spectroscopic temperatures were checked by visual inspection of Hα and Hβ line profiles, in comparison to stars of previously determined effective temperature. Surface gravity and v_t were then adjusted to maintain ionization balance and remove any trend of Fe I abundance with line strength, as necessary.

Stellar parameters for our program stars are presented in Table 2. Note that the metallicities are relative to the solar abundance from Asplund et al. (2009). We have also calculated 1D non-LTE (NLTE) log *g* and [Fe/H] values for the stars following the method described in Ruchti et al. (2013) and using the NLTE grid of Lind et al. (2012). These values are also given in Table 2.

Figure 2 shows the positions of the stars in this study in the Hertzsprung–Russell diagram. Twelve Gyr α-enhanced isochrones with [Fe/H] = −3.0, −2.5, −2.0, and −1.5 from Kim et al. (2002), and a 12 Gyr, [Fe/H] = −2.2 BaSTI horizontal branch isochrone (Pietrinferni et al. 2006) are also shown. Filled symbols indicate the LTE log *g* values, and open circles represent the NLTE log *g* values. As expected, log *g* values

[8] Generally, these candidates were photometrically selected more than once and given two different identifiers, and were only identified as duplicates during the high-resolution spectroscopic analysis.

[9] Recall the caveat in that paper that the calibration may not be valid for stars with [Fe/H] < −4.0. The lowest metallicity of any star in this sample is −4. We note that although this correction was not tested for stars with [Fe/H] > −2.5, such stars have been known to have similar discrepancies between their photometric and spectroscopic $T_{\rm eff}$ values (see, e.g., Johnson 2002).

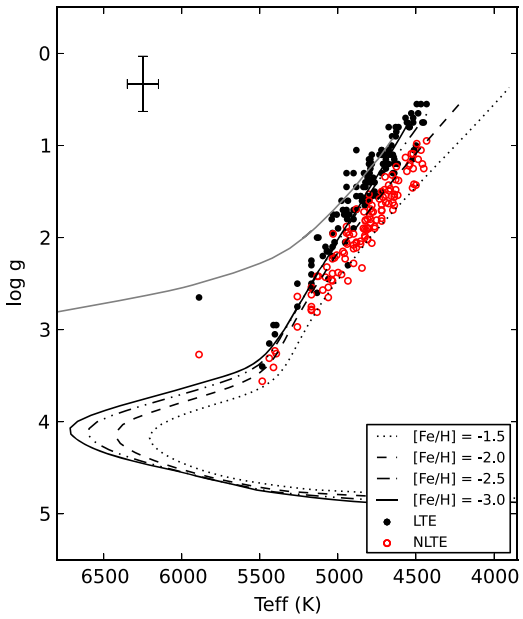

Figure 2. Hertzsprung–Russell diagram for the current sample, plotted with isochrones from Kim et al. (2002) and a horizontal branch isochrone from Pietrinferni et al. (2006). LTE parameters are shown as filled circles, and NLTE parameters are open red circles.

calculated in NLTE are ∼0.4–0.5 dex larger than the LTE gravities.

All the stars in this sample are giant stars, many of which lie on the upper part of the giant branch. While this means that the abundances of elements modified by stellar evolution (i.e., Li, C, N, O, s-process) will not reflect the primordial values of some of the stars, we do not have to worry about systematic differences in abundances between dwarfs and giants as found in some studies (see, e.g., Yong et al. 2013a). The likely reasons for the lack of dwarfs in this sample are discussed in S. Keller et al. (2015, in preparation).

3.2. Element Abundance Determination

EWs of lines in our line list were measured via fits of Gaussian profiles to absorption features in the spectra of the program stars. All measures were visually inspected. Any that were identified as outliers in the analysis process were further scrutinized and, where appropriate, adjusted or rejected. The Fe I and Fe II EWs were used to determine the stellar parameters (see Section 3.1); in high quality spectra of generally more metal-rich stars, ∼200 Fe I and ∼20 Fe II lines were used, while in the lower S/N star spectra, as few as 22 Fe I and ∼2 Fe II lines could be measured. Frebel et al. (2013) compared EW measures for lines in our line list using the same technique in this current work to literature measures for the standard star HD 122563. The agreement was excellent (differences less than 0.25 mÅ in the mean).

The stars subject to repeat observations also allow for a quantitative estimate of the robustness of our EW measures. For each star, the EW's measured from each spectrum were directly compared. The mean difference, in the sense $\Delta\mathrm{EW} = (\mathrm{EW1}-\mathrm{EW2}) \pm (\sigma/\sqrt{N})$, ranged from 0.5 ± 1.3 to 1.7 ± 0.5 mÅ, with standard deviations ranging from 8 to 29 mÅ.

The number of lines available for EW measurement varied widely for the other elements, with as many as 29 Ti I and 46 Ti II lines available, but typically only one line of, e.g., Al I and Si I. Chemical abundances for elements were determined using the measured EW values and the stellar parameters found from the iron lines. Table 3 gives the EW measures for all program stars, along with the measured logϵ abundances.

The following absorption features were analyzed via spectrum synthesis: 4313 Å, 4323 Å (CH, G-band); 4246 Å (Sc II); 4030 Å, 4033 Å, and 4034 Å (Mn I); 4077 Å, 4215 Å (Sr II); 4554 Å, 4934 Å (Ba II); and 4129 Å (Eu II). Additional Mn I and Sc II lines were synthesized for 54 stars in the sample, along with the Al I 3944 Å feature. In each synthesized region, the abundances of elements other than the one of interest were fixed to the value determined via EW.

Synthetic spectra were generated with MOOG and then convolved with a Gaussian to match the resolution of the MIKE spectra. Where necessary, the continuum-placement of the data was adjusted and the spectrum radial-velocity shifted to correct for subtle wavelength differences. Abundances were then determined by minimizing the difference between the observed and synthetic spectra by eye. The uncertainty of the spectral matching was then determined by decreasing the step size (in abundance space) between three synthetic spectra until the best match could no longer be uniquely identified. Example syntheses are given in Figure 3. Abundance results from spectrum synthesis (excluding CH) are also given in Table 3.

Element abundances of the stars in this sample are presented in Table 4, relative to the solar abundances of Asplund et al. (2009). Abundance upper limits obtained via spectrum synthesis are identifed as such in the table.

3.3. Error Analysis

The abundance uncertainties in our analysis are a combination of both random uncertainties (e.g., in the EW measures, etc.) and systematic uncertainties (due to continuum-placement, the adopted temperature scale, model atmosphere grid, etc.). Based on the spectroscopic techniques used here to determine the stellar parameters, we estimate their uncertainties to be ∼100 K, 0.3 dex and 0.2 km s^{-1} for $T_{\rm eff}$, log g and v_t, respectively. The contribution of each of these to the abundance uncertainty of each element was determined by varying each parameter by its uncertainty and recalculating the abundance. Table 5 lists the abundance uncertainties of individual elements for both a warmer and cooler example star from our sample. The random uncertainty (σ) listed in the third column is the standard error in the mean of individual line abundances for each element. In the cases where only one line was measureable, this value is placed conservatively at 0.2 dex, as appropriate for the low S/N of many of our "snapshot" spectra. The last column shows the quadratic sum of the individual uncertainties.

4. RESULTS

In this section, we review the abundance results for this SkyMapper sample for individual elements, divided roughly by group in the periodic table. Unless stated otherwise, the abundances presented here are LTE abundances.

First though, Figure 4 shows the distribution of metallicities of the SkyMapper metal-poor candidates in different observing campaigns. The top left panel shows only the 24 most metal-poor stars of the first 160 followed up with high-resolution spectroscopy, as previously discussed. The remaining panels

Table 3
Equivalent Width Measurements

Star	Wavelength	Species	E.P.	log gf	EW (mÅ)	log ϵ(X)
SMSS J000113.96–363337.9	3689.458	26.0	2.940	−0.168	82.3	5.12
SMSS J000113.96–363337.9	3753.611	26.0	2.180	−0.890	93.0	5.25
SMSS J000113.96–363337.9	3765.539	26.0	3.240	0.482	87.2	4.92
SMSS J000113.96–363337.9	3786.677	26.0	1.010	−2.185	96.0	5.19
SMSS J000113.96–363337.9	3805.343	26.0	3.300	0.313	74.2	4.81
SMSS J000113.96–363337.9	3839.256	26.0	3.050	−0.330	75.1	5.17
SMSS J000113.96–363337.9	3842.047	27.0	0.920	−0.770	66.4	2.70
SMSS J000113.96–363337.9	3845.169	26.0	2.420	−1.390	52.7	4.92
SMSS J000113.96–363337.9	3852.573	26.0	2.180	−1.180	81.8	5.18
SMSS J000113.96–363337.9	3881.869	27.0	0.580	−1.130	73.5	2.82
SMSS J000113.96–363337.9	3882.291	22.1	1.120	−1.710	81.4	3.15
SMSS J000113.96–363337.9	3885.510	26.0	2.420	−1.090	68.6	5.00
SMSS J000113.96–363337.9	3904.784	22.0	0.900	0.030	40.2	2.77
SMSS J000113.96–363337.9	3917.181	26.0	0.990	−2.155	108.9	5.41
SMSS J000113.96–363337.9	3924.526	22.0	0.020	−0.881	38.8	2.61
SMSS J000113.96–363337.9	3940.878	26.0	0.960	−2.600	77.0	4.96

(This table is available in its entirety in machine-readable form.)

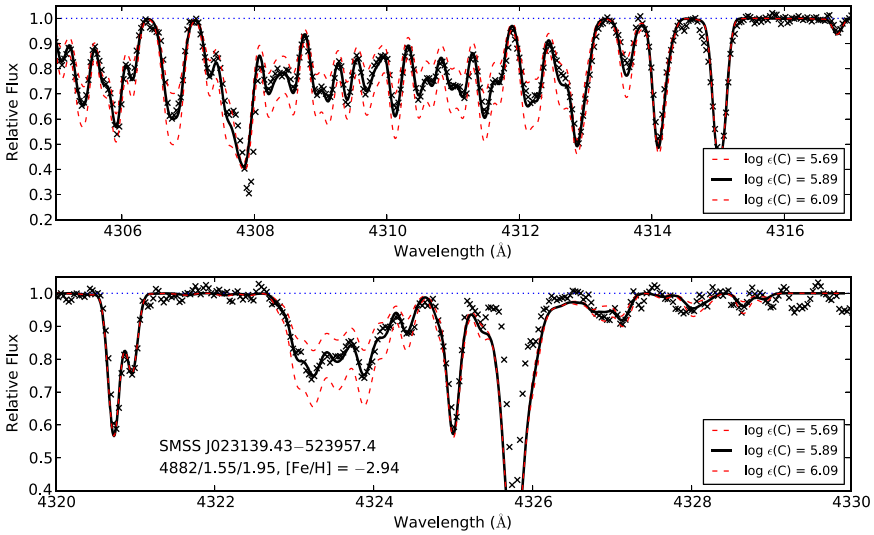

Figure 3. Syntheses of the CH bands at 4305–4317 Å (top) and 4320–4330 Å (bottom) in the star SMSS J023139.43–523957.4. Its stellar parameters are also listed as "$T_{\rm eff}$/log g/v_t." The synthetic spectra have C abundances varying in steps of 0.2 dex. The best fit, log ϵ(C) = 5.89, or [C/Fe] = +0.40, is the solid black line. Spectra with C abundances ± 0.2 dex around this value are shown as red dashed lines.

Table 4
Element Abundances

Star	logϵ(X)	# lines	s.d.	[X/H]	[X/Fe]
		C			
SMSS J000113.96–363337.9	5.78	2	0.02	−2.65	−0.33
SMSS J001039.86–525851.4	5.88	2	0.03	−2.55	−0.23
SMSS J001952.15–525803.0	5.62	2	0.02	−2.81	−0.25
SMSS J002148.06–471132.1	5.55	2	0.04	−2.88	0.29
SMSS J003055.81–482011.3	5.95	2	0.05	−2.48	0.05
SMSS J003327.36–491037.9	<4.67	1	0.00	< −3.75	< −0.40
SMSS J004037.56–515025.2	4.51	2	0.09	−3.92	−0.09
SMSS J005953.98–594329.9	5.70	2	0.05	−2.73	1.21
SMSS J010332.63–534654.3	5.59	2	0.09	−2.84	0.19
SMSS J010651.91–524410.5	4.77	2	0.05	−3.66	0.13

(This table is available in its entirety in machine-readable form.)

Table 5
Abundance Uncertainties Due to Atmospheric Parameters

Star	[X/Fe]	σ[a]	$\Delta T_{\rm eff}$(K) +100 K	Δlog g +0.3 dex	Δv_t +0.2 km s^{-1}	Δ[M/H] –0.25 dex	Total
SMSS J055746.51–575057.4	C I	0.02	+0.09	–0.08	+0.04	–0.06	+0.14
$T_{\rm eff}$ = 5404 K	Na I	0.03	+0.02	–0.08	–0.02	–0.01	+0.09
log g = 3.05	Mg I	0.03	–0.01	–0.05	+0.03	+0.00	+0.07
[Fe/H] = –2.50	Al I	0.20	+0.01	+0.00	+0.00	+0.00	+0.20
v_t = 1.45 km s^{-1}	Si I	0.20	+0.05	–0.12	+0.02	–0.02	+0.24
	Ca I	0.03	–0.04	+0.00	+0.01	–0.01	+0.05
	Sc II	0.07	–0.05	+0.12	–0.01	–0.01	+0.15
	Ti I	0.03	+0.01	+0.01	+0.02	+0.01	+0.04
	Ti II	0.02	–0.06	+0.11	–0.03	–0.01	+0.13
	Cr I	0.04	+0.01	–0.01	–0.03	+0.00	+0.05
	Mn I	0.06	+0.04	–0.03	–0.09	+0.00	+0.12
	Fe I[b]	0.01	+0.10	–0.02	–0.04	–0.01	+0.11
	Fe II[b]	0.03	+0.01	+0.12	–0.03	–0.02	+0.13
	Co I	0.04	+0.02	+0.01	–0.02	+0.00	+0.05
	Ni I	0.04	+0.01	–0.01	–0.05	+0.00	+0.07
	Zn I	0.20	–0.06	+0.08	+0.03	+0.00	+0.23
	Sr II	0.04	+0.00	+0.02	–0.07	–0.01	+0.08
	Ba II	0.10	–0.03	+0.10	–0.06	–0.01	+0.16
	Eu II	0.20	–0.07	+0.11	+0.05	+0.01	+0.24
SMSS J004037.56–515025.2	C I	0.13	+0.20	–0.09	+0.00	–0.02	+0.26
$T_{\rm eff}$ = 4468 K	Na I	0.11	+0.00	+0.01	–0.04	+0.00	+0.12
log g = 0.55	Mg I	0.04	–0.02	–0.05	–0.05	+0.01	+0.08
[Fe/H] = –3.83	Al I	0.20	–0.01	–0.07	–0.07	+0.00	+0.22
v_t = 2.45 km s^{-1}	Si I	0.20	+0.00	+0.01	+0.01	–0.01	+0.20
	Ca I	0.02	–0.05	+0.02	+0.02	–0.01	+0.06
	Sc II	0.20	–0.04	+0.11	+0.00	–0.01	+0.23
	Ti I	0.04	+0.01	+0.01	+0.03	+0.00	+0.05
	Ti II	0.02	–0.05	+0.12	+0.00	+0.00	+0.13
	Cr I	0.03	+0.02	–0.03	–0.04	+0.00	+0.06
	Mn I	0.16	+0.03	–0.01	+0.00	+0.00	+0.16
	Fe I[b]	0.01	+0.13	–0.05	–0.03	–0.01	+0.14
	Fe II[b]	0.03	+0.04	+0.09	–0.01	+0.00	+0.10
	Co I	0.03	+0.02	–0.02	–0.02	+0.00	+0.05
	Ni I	0.04	+0.01	–0.03	–0.05	+0.00	+0.07
	Zn I	0.20	–0.07	+0.09	+0.03	–0.01	+0.23
	Sr II	0.03	–0.02	+0.09	–0.07	+0.02	+0.12
	Ba II	0.13	–0.03	+0.11	+0.00	–0.01	+0.17
	Eu II	0.20	–0.14	+0.07	+0.03	–0.02	+0.26

[a] The standard error of the mean of individual line element abundances.
[b] These values are [X/H] ratios.

save the last include all of the stars observed in each campaign. Stars observed in multiple campaigns (see Table 1) are distributed according to their first observation date. The bottom right panel shows the distribution of the entire sample. In each panel, the mean and median [Fe/H] values are indicated by cyan solid and dashed lines, respectively.

As can be seen, the mean and median [Fe/H] values do not vary much from [Fe/H] ~ −2.8 in each panel, though the metal-poor tail is especially evident in the total sample (bottom right panel). Despite the fact that the photometric candidate selection technique was improved during the accumulation of this sample, no obvious improvement is seen in the distributions of the individual panels of Figure 4. This is largely due to the relative rarity of stars with [Fe/H] < −3.5 in the Milky Way halo and the necessity of observing more metal-rich targets due to the lack of more interesting metal-poor candidates in some runs (e.g., 2013 May). That said, 92 of the 122 stars (75%) have [Fe/H] ⩽ −2.5; 51 have −3 < [Fe/H] ⩽ −2.5 (42%); 32 have −3.5 < [Fe/H] ⩽ −3 (26%); and 9 have [Fe/H] ⩽ −3.5 (7%). Keep in mind these numbers have not been corrected for any biases. Indeed, since these candidates were selected from commissioning data, the distributions in Figure 4 should not be interpreted as *the* MDF of stars identified in the SkyMapper Survey. This will be the subject of future work.

4.1. Lithium

The Li I 6707 Å feature was detected in the spectra of 24 stars. We determined LTE Li abundances via spectrum synthesis using the line list of Hobbs et al. (1999) and assuming a pure ^{7}Li component. These are given in Table 6, along with measured EWs (in mÅ) and NLTE Li abundances calculated using the grid of Lind et al. (2009). Figure 5 shows log ϵ(Li) = A(Li) (LTE: crosses; NLTE: open circles) as a function of $T_{\rm eff}$ and [Fe/H], along with those of giant stars from the sample of Spite et al. (2005). (We only show their stars

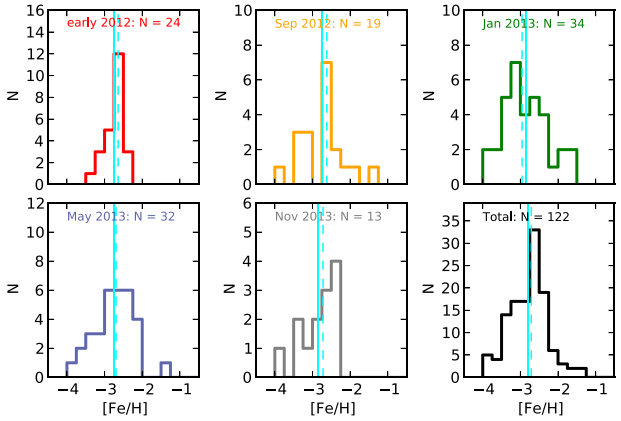

Figure 4. (LTE) metallicity distribution function of the Skymapper sample, separated by observation date, with the total sample in the bottom right-hand panel. The bin size is 0.25 dex everywhere. The mean and median [Fe/H] values are indicated by solid and dashed cyan lines, respectively. Note that the "early 2012" distribution is incomplete at [Fe/H] $\gtrsim -2.5$.

Table 6
Lithium Abundances of SkyMapper Stars

Star	EW (mÅ)	A(Li) (LTE)	A(Li) (NLTE)
SMSS J002148.06–471132.1	25.1	0.92	1.02
SMSS J005953.98–594329.9	70.1	2.00	1.97
SMSS J010839.58–285701.5	16.1	0.80	0.89
SMSS J015941.53–781408.7	16.2	0.76	0.85
SMSS J024858.41–684306.4	12.3	0.75	0.83
SMSS J031556.09–473442.1	32.7	1.08	1.13
SMSS J040148.04–743537.3	13.0	0.73	0.80
SMSS J051008.62–372019.8	15.1	1.00	1.04
SMSS J062609.83–590503.2	12.0	0.80	0.87
SMSS J070257.95–600422.4	22.3	0.91	1.02
SMSS J090247.43–122755.0	10.6	0.72	0.81
SMSS J105320.99–435300.1	13.6	0.80	0.87
SMSS J105438.86–435819.9	16.3	0.92	0.99
SMSS J121353.63–441911.2	24.3	0.85	0.93
SMSS J125115.37–331448.1	28.1	0.95	1.04
SMSS J141547.72–414034.0	19.1	1.00	1.06
SMSS J151101.05–182103.0	30.0	1.30	1.35
SMSS J155628.74–165533.4	13.1	0.70	0.80
SMSS J165219.76–253133.7	21.5	1.00	1.08
SMSS J174922.26–455103.8	24.1	0.85	0.97
SMSS J190549.33–214945.0	16.1	0.85	0.94
SMSS J193617.38–790231.4	23.0	1.16	1.21
SMSS J205313.80–651830.6	17.2	0.76	0.85
SMSS J215805.81–651327.2	23.8	0.81	0.90

with Li measures, no upper limits.) As can be seen, the distributions of Li abundances for the two samples are similar. The second most metal-poor star in our sample, SMSS J005953.98–594329.9 ([Fe/H]~ -4), has the largest Li abundance, A(Li) = 2.0 (LTE), but at a depletion level appropriate for its $T_{\rm eff}$. Note that NLTE corrections to the Li abundances are small for these stars: no more than 0.12 dex.

4.2. Carbon

During the ascent up the red giant branch, the surface C abundance of a star decreases due to dredge-up of CN-processed material. Placco et al. (2014b) provide C abundance corrections as a function of surface gravity and metallicity to take this effect into account. We have corrected the carbon

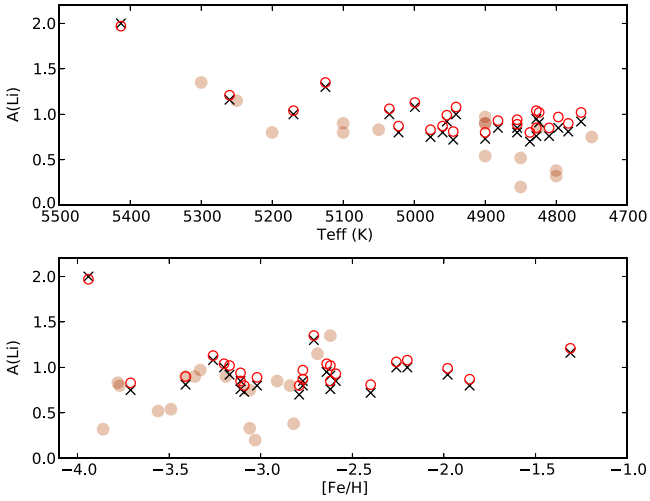

Figure 5. Li abundances of stars showing λ6707 absorption as a function of $T_{\rm eff}$ (top panel) and LTE [Fe/H] (bottom panel). LTE and NLTE abundances are shown as crosses and open circles, respectively. Giant stars with Li measures from the sample of Spite et al. (2005) are shown as filled red circles.

Table 7
Corrected Carbon Abundances

Star	[C/Fe]$_{\rm orig}$	Corr.	[C/Fe]$_{\rm corr}$
SMSS J000113.96–363337.9	–0.33	0.42	0.09
SMSS J001039.86–525851.4	–0.23	0.67	0.44
SMSS J001952.15–525803.0	–0.25	0.67	0.42
SMSS J002148.06–471132.1	0.29	0.49	0.78
SMSS J003055.81–482011.3	0.05	0.45	0.50
SMSS J003327.36–491037.9	< -0.40	0.72	< 0.33
SMSS J004037.56–515025.2	–0.09	0.71	0.62
SMSS J005953.98–594329.9	1.21	0.00	1.21
SMSS J010332.63–534654.3	0.19	0.50	0.69
SMSS J010651.91–524410.5	0.13	0.72	0.85

(This table is available in its entirety in machine-readable form.)

abundances of our sample stars accordingly since we are interested in the stars' natal carbon abundances and whether their birth gas clouds were particularly enhanced in carbon. In Table 7 we provide uncorrected and corrected [C/Fe] values. The corrections from Placco et al. (2014b) were calculated adopting [N/Fe] = 0.0.

Corrected carbon abundances are shown as crosses in Figure 6, along with upper limits as arrows. For comparison, in this and the following figures we plot our results against those of the *giant* stars in Yong et al. (2013a) (red circles, also corrected).[10] The bottom panel of Figure 6 shows [C/Fe] for this sample plotted against surface gravity. The carbon abundances exhibited by the SkyMapper sample are overall typical for stars found in the halo.

Also indicated in the figure is the definition for carbon-enhanced metal-poor (CEMP) stars of [C/Fe] $\geqslant 0.7$ (dotted line), following Aoki et al. (2007). Considering the corrected carbon abundances, we determine the frequency of CEMP stars

[10] We consider here the giant stars from both their literature compilation and their own sample. We note that the stellar parameter determination by Yong et al. (2013a) and the line list they used were different from those used here and so systematic differences between results may exist.

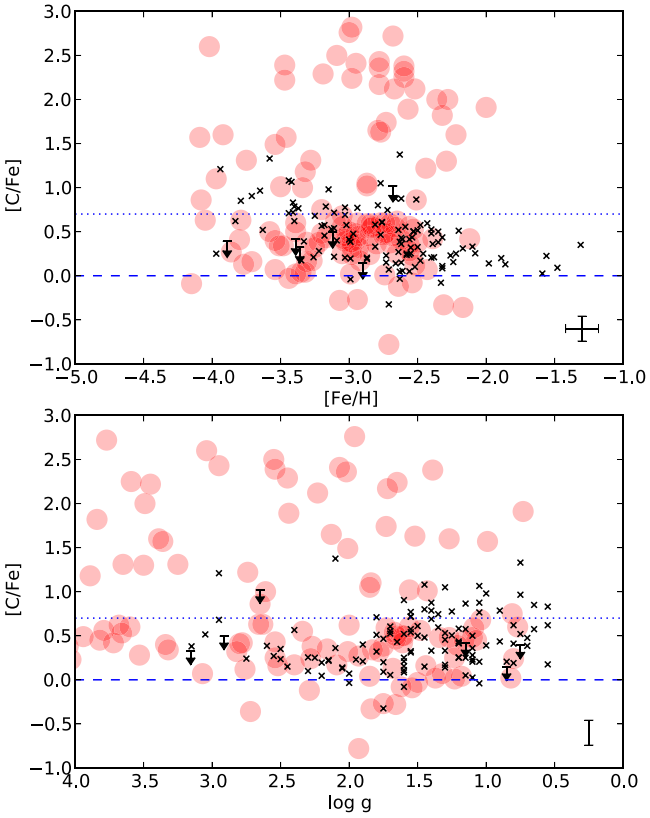

Figure 6. Top panel: corrected [C/Fe] abundances vs. (LTE) [Fe/H] for our sample (crosses) compared to the sample of Yong et al. (2013a) (red circles; also corrected). Upper limits are denoted by arrows. Bottom panel: corrected [C/Fe] abundances vs. surface gravity. The CEMP definition of Aoki et al. (2007) is indicated by a dotted line.

to be 20% (24/120) for the total sample. The frequency is 21% (24/113) for stars with [Fe/H] $\leqslant -2.0$, 26% (24/91) for [Fe/H] $\leqslant -2.5$, 39% (16/41) for [Fe/H] $\leqslant -3.0$, and 56% (5/9) for stars with [Fe/H] $\leqslant -3.5$. For comparison, using 505 metal-poor stars from the literature with [Fe/H] $\leqslant -2.0$ and corrected carbon abundances, Placco et al. (2014b) determined these frequencies to be 20%, 24%, 43%, and 60%, respectively. Our values agree very well with theirs. We note that CEMP-s and CEMP-rs stars have been excluded from the Placco et al. sample; since our sample does not contain any of these stars either, the comparison between these samples is appropriate.

Interestingly, our sample contains only seven stars with [C/Fe] > 1.0, of which five have [C/Fe] ~ 1.0. Star SMSS J173823.36–145701.0 has a corrected carbon abundance of [C/Fe] = 1.33, which is the highest in the sample. (Its uncorrected [C/Fe] is 0.60; the gravity is low, $\log g = 0.75$, which leads to the large correction.) It has [Fe/H] = −3.58. SMSS J005953.98–594329.9, at [Fe/H] = −3.94, has the second highest [C/Fe] ratio of +1.21 (no carbon correction because of $\log g = 2.95$). These two, together with the other five CEMP stars, are thus prominent examples of the CEMP-no group: they lack enhanced neutron-capture element abundances, and their other [X/Fe] ratios are comparable to those of typical halo stars at similar metallicities (Frebel & Norris 2015). Since five of the seven stars have [Fe/H] < -3.4, we confirm that CEMP-no stars preferentially appear at the lowest metallicities, i.e., below [Fe/H] < -3.0.

It is worthwhile asking why no stars with [C/Fe] $\gtrsim 2$ appear in our sample. Such stars typically exhibit large enhancements of s-process elements like Ba (CEMP-s stars, mentioned above). Very strong G-band absorption may change the colors of a star, moving it out of the range used for candidate selection. This is currently under investigation (S. Keller et al. 2015, in preparation).

4.3. Na and Al

Figure 7 presents the LTE [X/Fe] ratios for Na and Al versus LTE [Fe/H] for our sample. Also shown are the giant star sample from Yong et al. (2013a) and the Milky Way halo star literature sample from Frebel (2010; orange circles).[11] In this and the following figures, we have performed a linear regression analysis on the [X/Fe] versus [Fe/H] distributions of our sample in order to compare our results to other studies in the literature. Following Yong et al. (2013a), we restricted the sample to [Fe/H] $\leqslant -2.5$ and calculated the rms scatter of points about that fit. Stars with [X/Fe] ratios more than 2σ away from the fit were excluded and the linear regression redone. The resulting line of best fit, excluding the 2σ outliers, is shown in each panel (cyan line), along with its slope, the slope error, and the rms scatter about the slope. Also shown are the mean [X/Fe] ratios and standard deviations, the total number of stars, and the number of stars used in the fit.

As can be seen, the SkyMapper stars exhibit the >1 dex spread in [Na/Fe] found in other studies of metal-poor stars. The [Na/Fe] ~ 0 for stars with [Fe/H] > -2 is also consistent with other stars in this metallicity range. There is no significant change in [Na/Fe] as a function of [Fe/H], as indicated by the flat slope for stars with [Fe/H] $\leqslant -2.5$. A star's spectrum is often contaminated with Na D absorption from the interstellar medium. The 5889/5895 Å Na lines of stars with very small ($\lesssim$10 km s^{-1}) radial velocities were inspected for possible contamination with ISM features and were discarded when necessary.

We have calculated NLTE Na abundances as described in Lind et al. (2011). Five stars fell outside the grid of Lind et al. (2011), and therefore do not have NLTE abundances. We have confirmed with detailed calculations for a few stars that these NLTE abundances are appropriate at the level of ∼0.05 dex, in spite of differences in model atmospheres use in this work (Castelli & Kurucz 2004), and in Lind et al. (2011) (MARCS; Gustafsson et al. 2008). LTE abundances of this work were found to differ by up to 0.3 dex from those calculated using the method of Lind et al. (2011) for strong lines. Figure 8 plots LTE and NLTE [Na/Fe] values (crosses and open circles, respectively), versus LTE [Fe/H]. (Note that the NLTE [Na/Fe] values were calculated using both NLTE Na and Fe abundances.) The large (∼0.7–1 dex) differences reflect the negative (NLTE-LTE) corrections for Na and the positive (NLTE-LTE) corrections for Fe.

The Al abundances for our stars are based only on measurement of the 3961 Å Al I line for roughly half of the sample, while the other half included measurement of the 3944 Å feature. No systematic abundance offsets were found between stars with one and two measured features. Based on Figure 7, the LTE [Al/Fe] ratios of our sample are also

[11] In this and the following figures that include both the Yong et al. (2013a) and Frebel (2010) samples, all stars in the former sample have been excluded from the latter. The Frebel (2010) sample is a mixture of dwarf and giant stars.

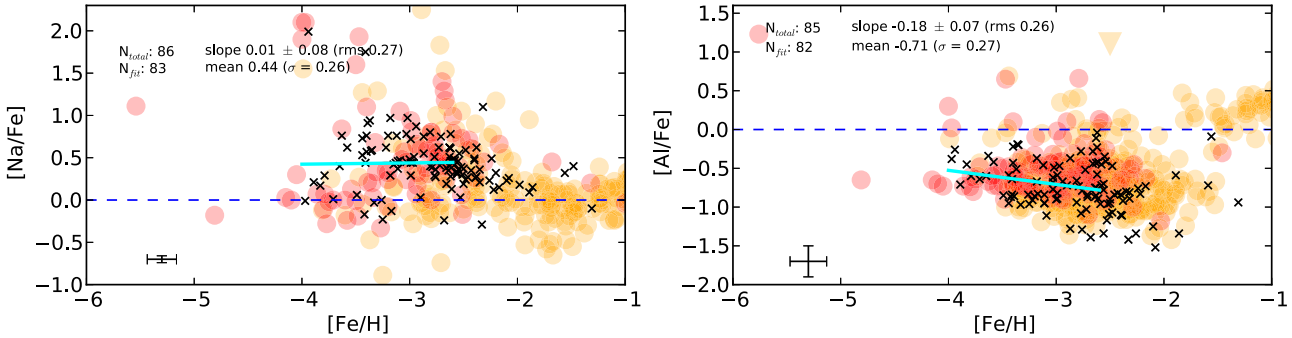

Figure 7. LTE [Na/Fe] and [Al/Fe] ratios vs. (LTE) [Fe/H] for the SkyMapper sample (crosses) compared to the sample of Yong et al. (2013a) (red circles) and the literature compilation of Frebel (2010) (orange circles). A least-squares fit to SkyMapper stars with (LTE) [Fe/H] $\leqslant -2.5$, excluding 2σ outliers, is indicated by the cyan line. Parameters of the least-squares fit are also given.

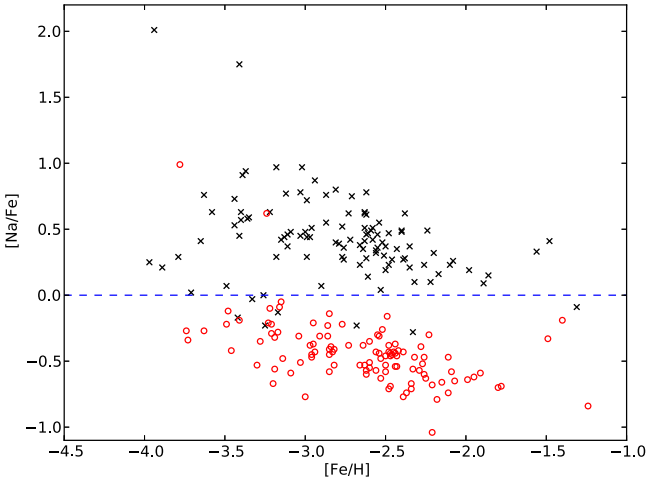

Figure 8. LTE [Na/Fe] (crosses) and NLTE [Na/Fe] (red open circles) plotted as a function of LTE [Fe/H] for the SkyMapper sample. Note not all stars have NLTE abundances. Differences between LTE and NLTE abundances are of order 0.7–1 dex. See the text for more information.

comparable to those of Yong et al. (2013a), though the standard deviation in [Al/Fe] is roughly 1.5 times as large as in their work. This is not surprising given the low S/N of some of our spectra, especially below 4000 Å. Baumueller & Gehren (1997) found NLTE corrections as large as +0.65 dex are necessary for Al abundances of cool, metal-poor stars. A correction of this magnitude would bring [Al/Fe] values in Figure 7 within ∼0.1 dex of solar. Such ratios are more consistent with predictions of chemical evolution models (e.g., Kobayashi et al. 2006) than the LTE stellar abundances, as has been noted before.

4.4. α-elements

The LTE [X/Fe] ratios for the α-elements (Mg, Ca, Si, Ti) versus LTE [Fe/H] are presented in Figure 9. Ti I and Ti II abundances[12] are plotted separately, with an additional panel that shows the difference between them as a function of metallicity. As can be seen, the agreement between them is good, with the mean difference comparable to the dispersion about the means of both species. This is similar to the agreement found by Yong et al. (2013a) for their giant star sample.

[12] Strictly, these are $[\mathrm{Ti/Fe}]_{\mathrm{Ti\,I}}$ and $[\mathrm{Ti/Fe}]_{\mathrm{Ti\,II}}$, but we denote them as [Ti I/Fe] and [Ti II/Fe] for convenience.

Looking more closely, Ti I and Ti II abundances have different slopes in Figure 9, while the difference between them at low [Fe/H] is different from that at high [Fe/H] (bottom right). The cause of these features is illustrated in Figure 10, where the difference between Ti II and Ti I abundances is plotted against the number of Ti I lines measured per star. As can be seen, the scatter in Δ[X/Fe] increases by a factor of two when N(Ti I) $\leqslant$ 5 and that the most metal-poor stars preferentially have fewer measurable Ti I lines. A star in our sample has an average of 30 Ti II lines measured in its spectrum, compared to only 13 Ti I lines. Consequently, the [Ti II/Fe] ratios in Figure 9 are more reliable. For stars that have N(Ti I) > 5, $([\mathrm{Ti\,II/Fe}] - [\mathrm{Ti\,I/Fe}]) = 0.11 \pm 0.10$.

We do not apply NLTE corrections to any α-element abundances for our sample, but summarize the magnitudes of corrections appropriate for our stars. NLTE corrections for Ti II abundances are expected to be ∼0.05 dex or less, while corrections for Ti I abundances are larger for metal-poor stars (+0.1–0.2 dex; Bergemann 2011). The difference between our LTE Ti II and Ti I abundances are consistent the magnitude of these corrections. Uncertainties in atomic data for individual lines likely also impact the scatter in abundances for both species, though we note that improved atomic data are now available (Lawler et al. 2013; Wood et al. 2013). NLTE corrections for Mg are at the level of ∼0.1 dex (Gehren et al. 2004; Mashonkina 2013), while for Ca I lines they can be as large as +0.3 dex for stars like those in our sample (Mashonkina et al. 2007, but see also Starkenburg et al. 2010).

Overall, the SkyMapper targets exhibit typical halo star abundance patterns, with relatively small (∼0.1 dex) dispersion in, e.g., Mg, Ca, and Ti abundances, and larger scatter in Si. These dispersions are comparable to or smaller than the standard deviations of individual line abundances for most stars in our sample. The intrinsically small dispersion in α-element abundances over a wide range of metallicity is well-documented in the literature (e.g., Cayrel et al. 2004) and implies that their nucleosynthetic yields have remained remarkably constant throughout the earliest phases of chemical evolution in the universe. The larger scatter in Si abundances is at least partly due to the difficulty in obtaining a robust measure for this element; for many stars in our sample it is based solely on one weak Si line (at 4102.9 Å, on the wing of Hδ) that was not measurable in all stars. The blended 3905 Å Si I line was analyzed via spectrum synthesis in a portion of our sample; no systematic offset between abundances of stars based on one or both lines was observed. In addition to the very small (<0.1 dex) dispersion in [X/Fe] versus [Fe/H] in metal-poor

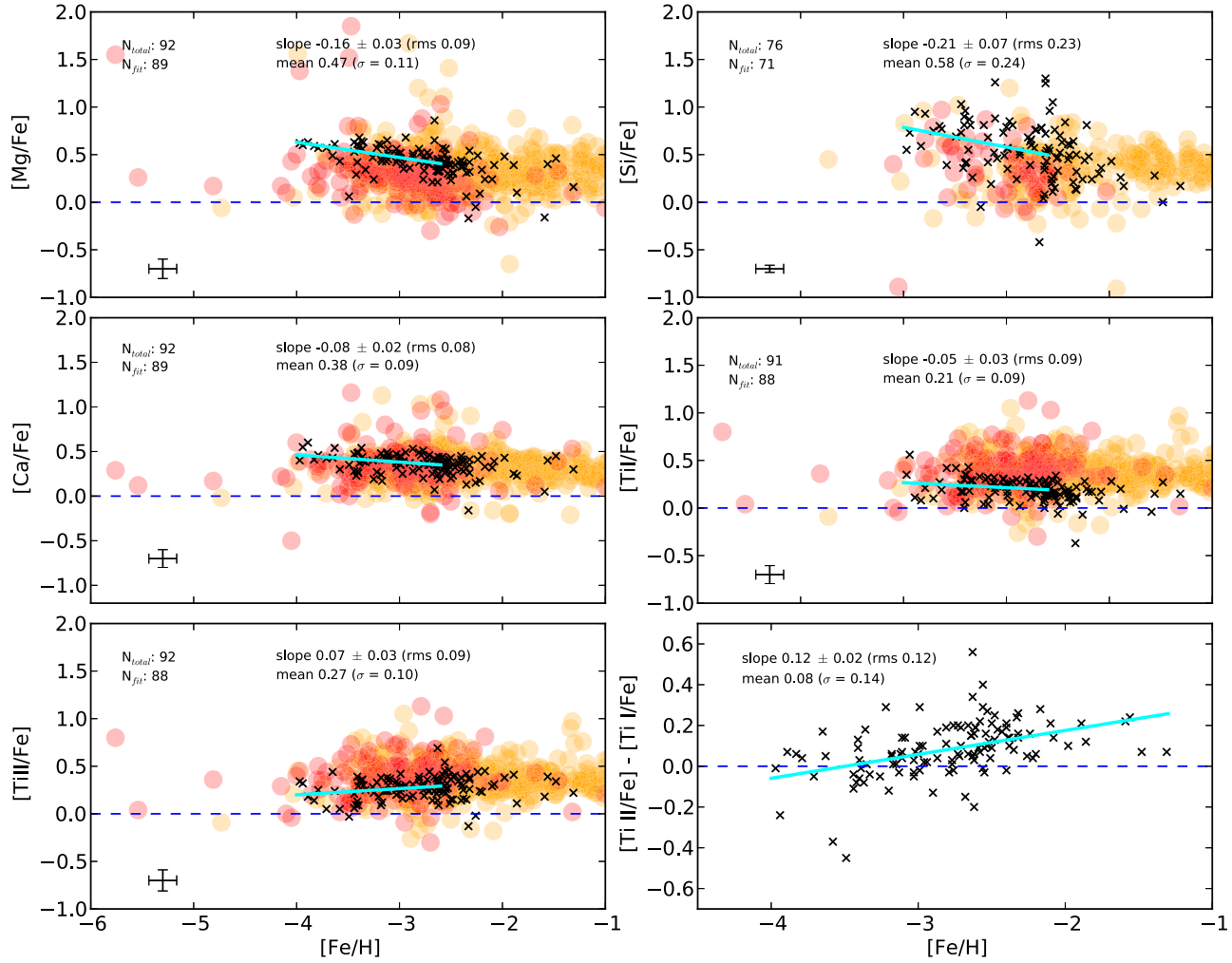

Figure 9. Same as Figure 7, but for the α-elements.

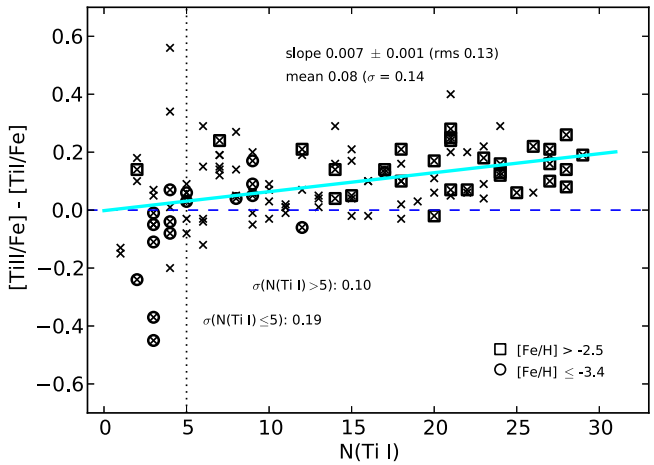

Figure 10. [Ti II/Fe] – [Ti I/Fe] differences vs. the number of Ti I lines measured in each star. There is a marked increase in scatter when N(Ti I) $\leqslant$ 5 (dotted line). The most metal-poor ([Fe/H]$\leqslant -3.4$) and metal-rich ([Fe/H] > -2.5) stars are indicated by circles and squares, respectively. See text for more information.

stars, previous studies have found that the α-elements show flat trends with slopes consistent with zero. For all the α-elements in Figure 9 save Mg the magnitudes of the slopes are equivalent to the rms scatter.

4.5. Fe-peak Elements

Figure 11 shows the trends with [Fe/H] for the Fe-peak elements Sc, Cr, Mn, Co, Ni, and Zn.

As mentioned previously, Sc abundances are based on spectrum synthesis of only the Sc II 4246 Å line for ~40 stars in our sample, while for the remaining ~50 as many as four other lines were also analyzed. A comparison of the Sc II abundance determined from the 4246 Å line to the mean abundance of the other lines found a 0.08 dex ($\sigma = 0.19$) offset, in the sense that the other line abundances were larger. We have therefore added 0.08 dex to the Sc II abundance for stars in which only the 4246 Å line was measured.

There is an unexplained systematic offset in the zero-point of our Sc abundances compared to that of Yong et al. (2013a): our mean [Sc/Fe] = –0.11 is ~0.3 dex lower than the value for their giant sample, although the values are comparable within the standard deviations of the two samples (0.17 dex for ours, and 0.14 dex for theirs; see their Figure 22). This offset is also visible relative to the larger literature compilation and in our analysis of the standard star HD 122563 compared to literature studies (see Section 5.2). Yong et al. (2013a) include hyperfine splitting in their Sc analysis, as we do here. There is an 0.08 dex difference between their adoped log *gf* for Sc II 4246 (Kurucz & Bell 1995) and ours (Lawler & Dakin 1989), which is accounted for by our 0.08 dex

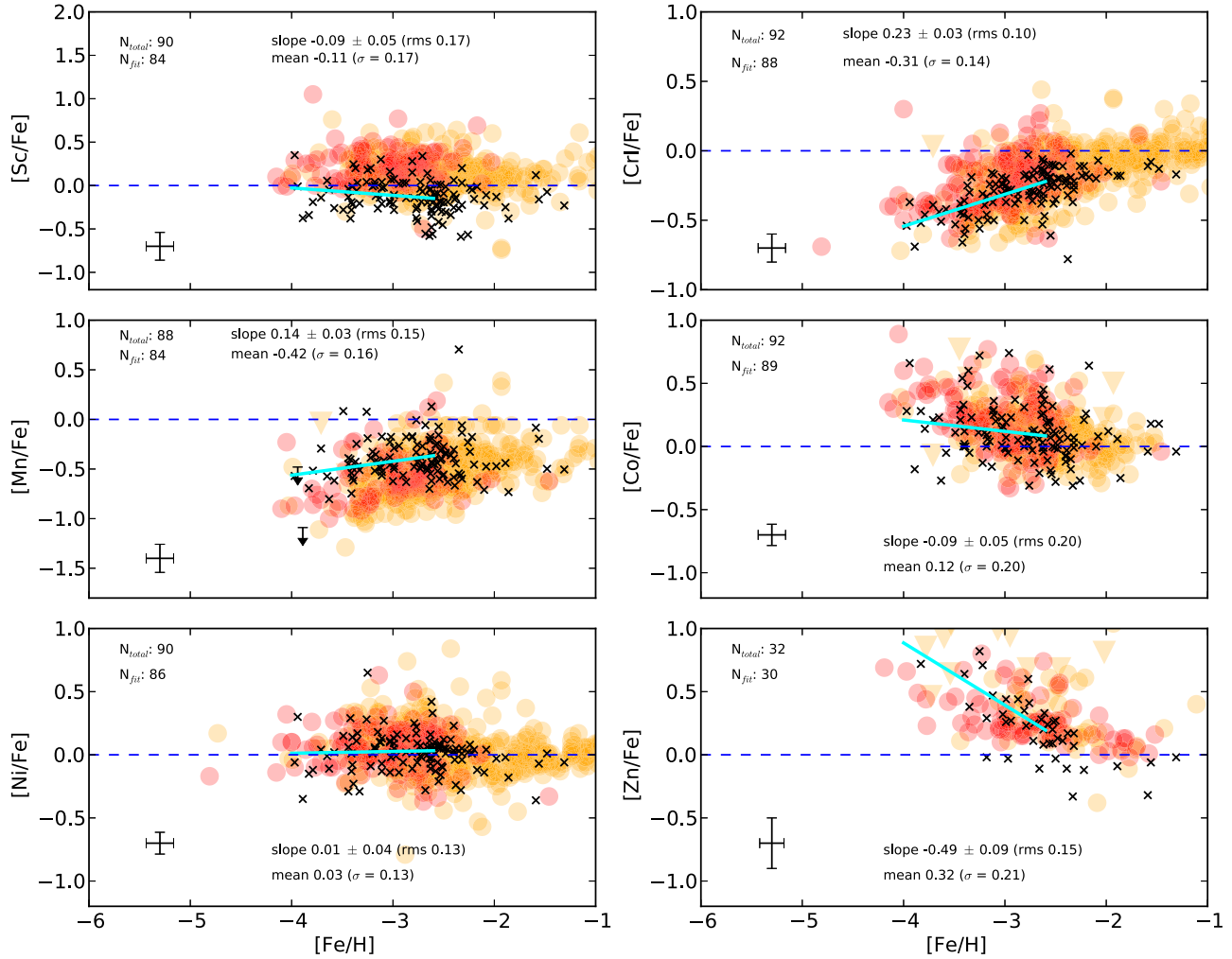

Figure 11. Same as Figure 7, but for the Fe-peak elements. For Zn (bottom right panel), the red symbols are those of Cayrel et al. (2004) and Barklem et al. (2005), while for the remaining elements they are from Yong et al. (2013a). As in other figures, the orange symbols are from Frebel (2010). Literature sample upper limits are shown as triangles.

correction to that line's abundance. Differences in log *gf* values from the above sources for the other lines considered here range from +0.03 to −0.20, and if anything, should make our abundances slightly larger than those of Yong et al. (2013a).

Cayrel et al. (2004) and Lai et al. (2008), among others, found that the Mn I λ4030 resonance lines had lower abundances than other Mn I lines by as much as 0.4 dex. For the ∼40 stars in which we measured both resonance and non-resonance Mn I lines, we found a difference of Δ(non-res.–res.) = +0.44 (s.e.m. 0.03) dex. We have therefore applied a +0.44 dex correction to the abundances measured from the Mn I 4030, 4033 and 4034 Å lines in all stars. Bergemann & Gehren (2008) have demonstrated that the systematic offset between resonance and non-resonance Mn I lines can be explained by NLTE effects. They found NLTE corrections for resonance lines as large as ∼ +0.7 dex for warm, metal-poor stars, while corrections for other Mn I lines as large as +0.4 dex are possible. NLTE [Mn/Fe] ratios for this SkyMapper sample would therefore be much closer to the solar ratio.

As for the general abundance distributions shown in Figure 11, the SkyMapper stars have the same trends of [X/Fe] versus [Fe/H] and the same scatter as the literature samples. The scatter with [Fe/H] is smallest for Cr and Ni, while Mn and Co show (opposite to each other) trends of [X/Fe] with [Fe/H]. Cayrel et al. (2004) remarked upon the similar behavior of [Cr/Fe] and [Mn/Fe] increasing with increasing [Fe/H] for their sample (both with quite small scatter), and the same can be seen in the Yong et al. (2013a) giant sample. In our sample, [Cr/Fe] and [Mn/Fe] values show similar trends with comparable scatter (∼0.15 dex). We also note that our mean [X/Fe] values for Cr, Co, and Ni agree very well with those of Yong et al. (2013a), while our mean [Mn/Fe] = −0.42 is ∼0.15 dex larger than theirs. As Yong et al. (2013a) did not include Zn, the literature sample we plot in the bottom right panel of Figure 11 is that of Cayrel et al. (2004) and Barklem et al. (2005). The SkyMapper stars show a similar trend and scatter in [Zn/Fe] as in those samples, however, we have found more stars exhibiting subsolar [Zn/Fe] ratios.

One star in Figure 11 exhibits an [X/Fe] ratio very different from the rest of the SkyMapper and literature samples. SMSS J093829.27–070520.9 appears to have [Mn/Fe] ∼ +0.7. However, its spectrum has S/N ∼10 at λ4000, and this abundance is based on measurement of only two Mn I resonance lines and has a standard deviation of 0.49 dex. Consequently, its enhanced [Mn/Fe] ratio should be treated with skepticism.

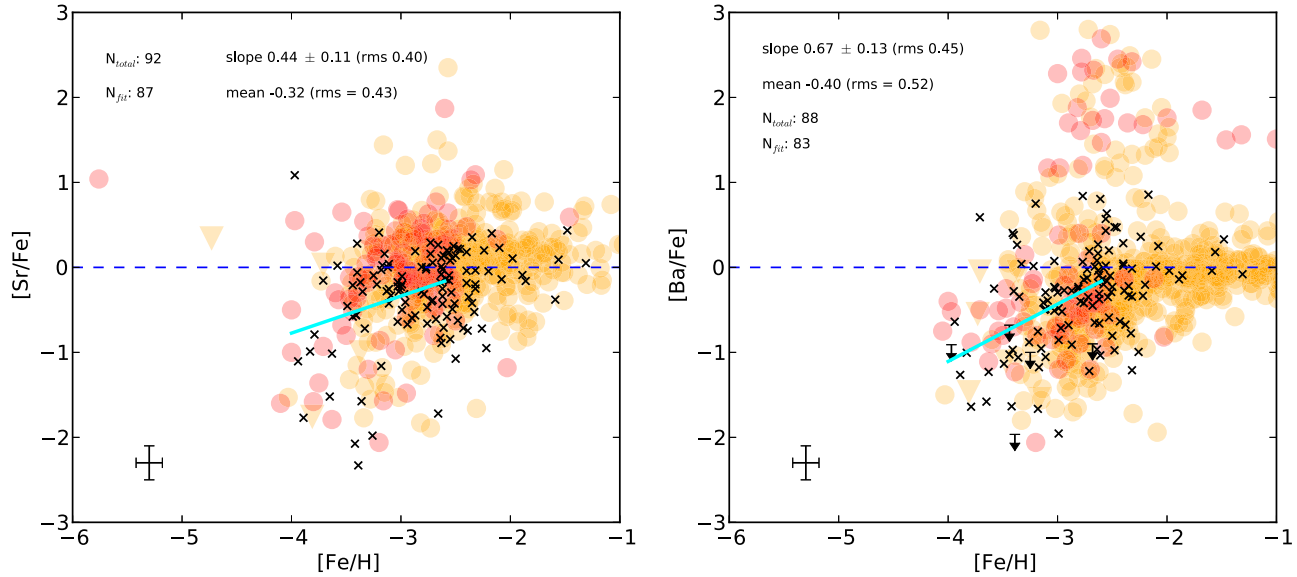

Figure 12. Same as Figure 7, but for Sr and Ba. Upper limits are denoted by arrows and triangles for our sample and the literature sample, respectively.

4.6. Neutron-capture Elements

The neutron-capture species considered in this analysis are Sr, Ba, and Eu. The first two are predominantly formed via the s-process in low-mass AGB stars, while Eu is almost entirely formed via the r-process (Sneden et al. 2008; Jacobson & Frebel 2014). The large variation of [X/Fe] versus [Fe/H] (>1 dex) for neutron-capture elements, in strong constrast to the relative constancy of the α-elements, has also been well-established in the literature (Aoki et al. 2005; Barklem et al. 2005; Lai et al. 2008; Roederer et al. 2010a, 2014a; Cohen et al. 2013; Roederer 2013; Yong et al. 2013a; Spite & Spite 2014). Our sample shows similar behavior (Figure 12). Over the ∼2.5 dex range of [Fe/H] spanned by our sample, there is evidence of the dispersion in [X/Fe] increasing with decreasing [Fe/H] as found in the literature (2–3 dex below [Fe/H] = −3 compared to 1–2 dex at higher [Fe/H] for Sr and Ba in Figure 12). We have found no s-process stars in our sample, even though the mean [Fe/H] of our sample is that of typical s-process metal-poor stars (e.g., Placco et al. 2013). This is consistent with the lack of stars with [C/Fe] $\gtrsim$ +2, which along with enhanced [s/Fe], is a signature of pollution from an AGB companion (Section 4.2).

The top panel of Figure 13 shows the [Sr/Ba] ratios for our sample as a function of their [Ba/Fe], which compares the relative abundances of light and heavy neutron-capture elements. Except for the star SMSS J022423.27–573705.1 which has [Sr/Ba] > 2 (see Section 5.2), our sample follows the same behavior as those of, e.g., Spite & Spite (2014) and Cohen et al. (2013). The Ba-poor objects show the largest range of [Sr/Ba] ratios, while the most Ba-rich objects show less scatter. There are three Ba-poor stars (with [Ba/Fe] < −1.0) that exhibit the solar system r-process [Sr/Ba] = −0.5. The Eu 4129 Å line was not measureable in any of their spectra; therefore, if they do follow the solar system r-process pattern, their level of r-process element enrichment would be extremely low. The upper limits to their [Eu/Fe] ratios are less than 0.4, at which level they would just be considered r-I stars (see below).

Based on a large literature sample, Aoki et al. (2013b) recently claimed that there is a dearth of stars with measurable [Sr/Ba] ratios below [Fe/H] < −3.5. Placco et al. (2014a) suggested this was due to the small/incomplete sample of stars in this metallicity regime; the bottom panel of Figure 13 lends support to this argument (see also Li et al. 2015). Roughly half of the stars below [Fe/H] < −3.5 exhibit large ($\gtrsim$1) [Sr/Ba] ratios.

We detected the Eu 4129 Å feature in a number of our MIKE spectra, and obtained upper limits on the Eu abundances for all other stars for which it was not detected. These abundances are shown in Figure 14. As Eu abundances were not included in the study of Yong et al. (2013a), we only include the Frebel (2010) literature sample in Figure 14. Again, we see a distribution of [Eu/Fe] with [Fe/H] in our study similar to that in the literature. Note that most of our Eu abundances are upper limits (denoted as arrows).

R-process enhanced stars are identified based on their Eu abundance: strongly r-process enhanced so-called r-II stars have [Eu/Fe] > 1.0, while mildly r-process enhanced r-I stars have 0.3 $\leqslant$ [Eu/Fe] $\leqslant$ 1.0 (and both classes have [Ba/Eu] < 0; Barklem et al. 2005). These values are indicated with dotted lines in Figure 14. Of the stars in our sample for which we have bona fide Eu measures, 4 have [Eu/Fe] $\geqslant$ 1, while another 22 qualify as r-I stars. The metallicity range of the r-II stars is −2.77 $\leqslant$ [Fe/H] $\leqslant$ −2.17. The star with the largest enhancement ([Eu/Fe] = +1.75), SMSS J175046.30–425506.9, also happens to be the most metal-rich of the r-II stars. Further analysis of these r-process enhanced stars is ongoing.

We end the discussion with some remarks about NLTE effects on the neutron-capture element abundances of metal-poor stars. NLTE Sr II abundances are expected to differ from LTE values by no more than 0.1 dex in the relevant stellar parameter regime (Andrievsky et al. 2011; Bergemann et al. 2012a). NLTE corrections to Ba II abundances (from, e.g., the λ4554 line) can range from roughly −0.10 to +0.25 dex, and are dependent upon the Ba abundance (Andrievsky et al. 2009). However, as noted by, e.g., Cohen et al. (2013) and Andrievsky et al. (2009), the magnitude of the scatter in metal-poor star Sr and Ba abundances is far greater than can be attributed to NLTE effects, and so they have little bearing on any interpretation of the data. NLTE Eu abundances

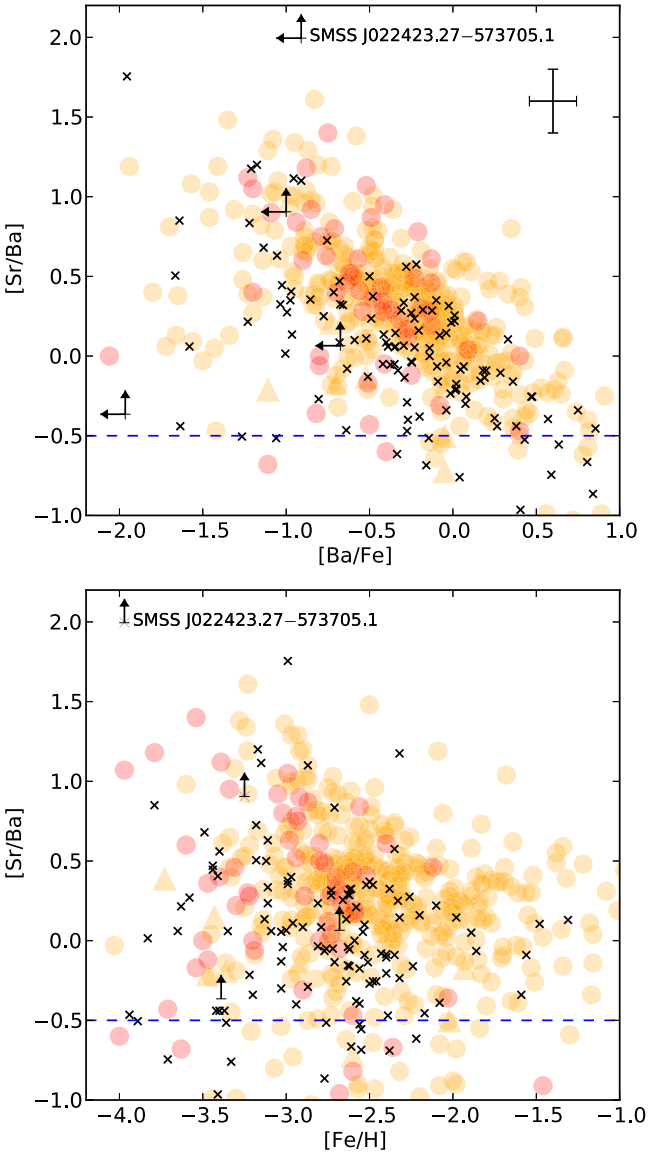

Figure 13. [Sr/Ba] vs. [Ba/Fe] (top) and [Fe/H] (bottom) for our sample and literature stars. A conservative errorbar of 0.2 dex in [Ba/Fe] and 0.28 dex in [Sr/Ba] is indicated in the upper right. The location of SMSS J022423.27–573705.1, which exhibits the largest [Sr/Ba] ratio of our sample (Section 5.2) is labeled in both panels. The range of [Sr/Ba] increases with decreasing [Ba/Fe], but some Ba-poor stars with the solar r-process [Sr/Ba] = −0.5 (dashed line) ratio are also present. Though the number of stars with [Fe/H] < −3.5 is small, their presence is at odds with recent claims that there is a cut-off in [Sr/Ba] in this metallicity range Aoki et al. (2013b).

can be larger than the LTE values by as much as ∼0.1 dex (Mashonkina et al. 2003), though to our knowledge Eu NLTE calculations have been done for dwarf stars only.

4.7. Known Stars Recovered by SkyMapper

The coordinates of all the stars in Table 1 were uploaded to the Simbad[13] database to check for any that have been previously studied. We used a search radius of 30″ around the stellar coordinates. Eight stars were found to have an entry in the database: four stars were found in the RAdial Velocity Experiment survey (RAVE; data release 4) (Kordopatis et al. 2013), three were found in various Hamburg-ESO survey

[13] http://simbad.u-strasbg.fr/simbad/

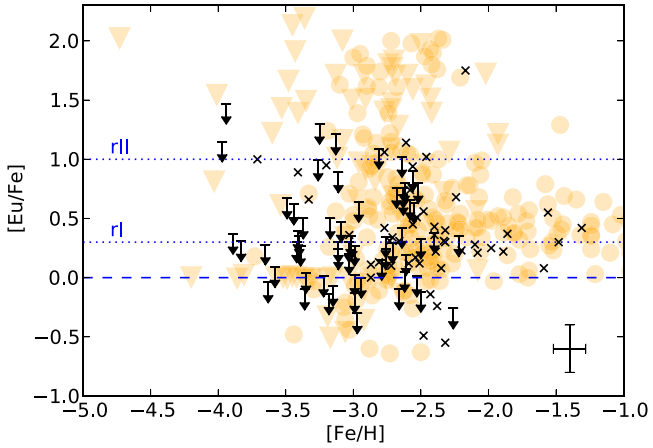

Figure 14. [Eu/Fe] vs. [Fe/H] for our sample (crosses) compared to the Frebel (2010) literature compilation (orange symbols). Upper limits are indicated as arrows or triangles. The [Eu/Fe] ranges for r-process enhanced (r-II and r-I) stars are indicated by dotted lines.

studies, and the last is identified (as a star) in the Millennium Galaxy Catalogue (Liske et al. 2003). Table 8 lists these stars along with their alternate identifications and reference studies.

The two most metal-poor stars in our sample, SMSS J022423.27–573705.1 and SMSS J005953.98–594329.9 (with [Fe/H] = –3.97 and –3.94, respectively), are in fact rediscoveries. SMSS J005953.98–594329.9 was included in the sample of Norris et al. (2013) and Yong et al. (2013a), and our stellar parameters and element abundances for this star are in excellent agreement with their values. SMSS J022423.27–573705.1 was identified in the RAVE survey, but the stellar parameters found by Kordopatis et al. (2013) are very different from ours: $T_{\rm eff}$/log g/[Fe/H] = 3600/4.5/–0.63 as opposed to 4846/1.60/–3.97.

Stellar parameters are determined from RAVE $R \sim 7500$ spectra (λ8410–8795) using sophisticated algorithms that match the data to a grid of synthetic spectra (Kordopatis et al. 2013). Kordopatis et al. (2013) give a set of stellar parameters and data characteristics (S/N, radial velocity measurement error, etc.) that serves as quality checks to ensure the results of the RAVE pipeline are robust and reliable. SMSS J022423.27–573705.1 fails to meet both the S/N (>20 pixel^{-1}) and the $T_{\rm eff}$ (>3800 K) requirements. Of the three other RAVE stars in our sample (Table 8), two meet all quality criteria while the RAVE pipeline did not converge for SMSS J010839.58–285701.5. For the two stars that pass muster, our $T_{\rm eff}$ values agree within 180 K of the RAVE values and our [Fe/H] values agree within 0.15 dex. Differences between log g values are quite large, however: 0.6 and 2.4 dex for SMSS J003055.81–482011.3 and SMSS J224843.95–543610.1, respectively. No systematic offset in any parameter is present. SMSS J215805.81–651327.2 and SMSS J010651.91–524410.5 were studied by Cayrel et al. (2004) and Barklem et al. (2005), respectively. For the former, our stellar parameters agree very well with those of Cayrel et al. (2004), within 120 K, 0.15 dex, 0.25 km s^{-1}, and 0.1 dex in $T_{\rm eff}$, log g, v_t, and [Fe/H], respectively. The agreement with Barklem et al. (2005) is not as good in the case of SMSS J010651.91–524410.5: our $T_{\rm eff}$ is 250 K cooler, and our log g and [Fe/H] values are 0.7 and 0.4 dex lower, respectively.

Table 8
Rediscovered EMP Stars from the Literature

SMSS ID	Literature ID(s)	References
SMSS J003055.81–482011.3	RAVE J003055.8–482011	Kordopatis et al. (2013)
SMSS J005953.98–594329.9	HE 0057–5959	Norris et al. (2013); Yong et al. (2013a)
SMSS J010651.91–524410.5	HE 0104–5300	Barklem et al. (2005)
SMSS J010839.58–285701.5	RAVE J010839.6–285701	Kordopatis et al. (2013)
SMSS J022423.27–573705.1	RAVE J022423.3–573705	Kordopatis et al. (2013)
SMSS J100251.13–000152.1	2MASS J10025112–0001520	Liske et al. (2003)
SMSS J215805.81–651327.2	CS 229656–050	Cayrel et al. (2004)
SMSS J224843.95–543610.1	RAVE J224844.0–543610	Kordopatis et al. (2013)

Table 9
Linear Regression Results

	This Study			Yong et al. (2013a)			Cayrel et al. (2004)			Cohen et al. (2013)		
[X/Fe]	Slope	Error	rms (dex)	Slope	Error	rms (dex)	Slope	Error	rms (dex)	Slope[a]	Error	rms (dex)
Na I	+0.01	0.08	0.27	+0.30	0.07	0.21	+0.403	0.010	0.25	…	…	…
Mg I	−0.16	0.03	0.09	−0.03	0.04	0.13	+0.035	0.003	0.13	+0.00	…	0.17
Al I	−0.18	0.07	0.26	+0.11	0.06	0.17	+0.047	0.005	0.18	−0.06	…	0.24
Si I	−0.21	0.07	0.23	−0.30	0.18	0.26	+0.032	0.004	0.15	−0.18	…	0.20
Ca I	−0.08	0.02	0.08	+0.02	0.03	0.10	+0.074	0.002	0.10	+0.00	…	0.15
Sc II	−0.09	0.05	0.17	+0.08	0.05	0.13	+0.034	0.002	0.11	+0.04	…	0.14
Ti I	−0.05	0.03	0.09	−0.10	0.04	0.11	−0.014	0.001	0.09	+0.14	…	0.14
Ti II	+0.07	0.03	0.09	+0.14	0.04	0.13	−0.014	0.001	0.09	+0.14	…	0.14
Cr I	+0.23	0.03	0.10	+0.15	0.03	0.10	+0.117	0.000	0.05	+0.24	…	0.13
Mn I	+0.14	0.03	0.15	+0.33	0.06	0.15	+0.030	0.003	0.12	+0.24	…	0.16
Co I	−0.09	0.05	0.20	−0.38	0.04	0.04	−0.131	0.002	0.13	−0.20	…	0.16
Ni I	+0.01	0.04	0.13	−0.02	0.04	0.13	−0.003	0.002	0.11	−0.06	…	0.21
Zn I	−0.49	0.09	0.15	…	…	…	−0.271	0.002	0.11	+0.00	…	0.25

Note.
[a] Slope calculated subtracting ⟨[X/Fe]⟩ values at [Fe/H] = −3.0 from values at [Fe/H] = −3.5 in Table 13 of Cohen et al. (2013).

As for radial velocity measures, our value for SMSS J005953.98–594329.9 agrees with that found by Norris et al. (2013) within 1.4 km s^{-1}. For SMSS J010651.91–524410.5 our measure is 3.7 km s^{-1} larger than in Barklem et al. (2005), while Cayrel et al. (2004) do not provide a radial velocity measurement for SMSS J215805.81–651327.2. For those stars in common with RAVE, our measures are −22 (for SMSS J022423.27–573705.1) to +23 (for SMSS J003055.81–482011.3) km s^{-1} different, in the sense (This Study—RAVE). Our measure for SMSS J010839.58–285701.5 is 7.5 km s^{-1} smaller than RAVE's, while there is only a 0.4 km s^{-1} difference for SMSS J224843.95–543610.1. According to Kordopatis et al. (2013), radial velocities measured from RAVE spectra in the S/N range of these stars (∼10–40) agree within 5–8 km s^{-1} to literature values, though differences as large as ∼20 km s^{-1} are possible (their Figure 34). Given the long baseline between our measures and theirs (the RAVE observations were taken in 2004 and 2006), it is possible that at least SMSS J003055.81–482011.3 and SMSS J022423.27–573705.1 are binary systems.

4.8. Comparison to Literature Samples

A quantitative comparison of our analysis to those of other studies can be made by inspection of the linear regression analyses carried out by different groups on different samples. The results of the regression analysis on this SkyMapper sample have been included in Figures 7–12; for convenience, they are presented in Table 9 along with those of Cayrel et al. (2004), Cohen et al. (2013), and Yong et al. (2013a). Figure 15 presents the values from Table 9 graphically.[14] The errorbars on the points represent the uncertainty of the slope, as given in this work and those of Yong et al. (2013a) and Cayrel et al. (2004) (we note that the slope uncertainties in the latter are smaller than the symbol in the figure).

Generally, the numerical values of the slopes in our analysis agree with those of the literature studies within 2σ for most of the elements presented here. Some elements show a large range of slopes: namely Na, Mg, Al, Co, and Zn. Another way of comparing results from different studies is to compare the mean [X/Fe] ratios found for stars with [Fe/H] < −2.5, and this is shown Table 10. The bottom panel of Figure 15 shows the difference between the [X/Fe] ratio found for a particular stellar sample and the mean ⟨[X/Fe]⟩ ratio of the four studies in Table 10. The errorbars on the points are the standard errors of the mean. Here one can see evidence of the systematic offsets between our study and others for some elements noted earlier, namely for Sc. For most of the elements, however, the mean [X/Fe] ratios found by different studies agree within a factor of two of their standard errors, though our Na and Mg values are higher than those of the other samples considered here.

[14] All groups considered here confined their regression analysis to stars with [Fe/H] < −2.5. Note that the slopes given for Cohen et al. (2013) in Table 9 were calculated using [X/Fe] ratios at [Fe/H] = −3 and [Fe/H] = −3.5 for their CEMP-no stars (columns 3 and 4 in their Table 13).

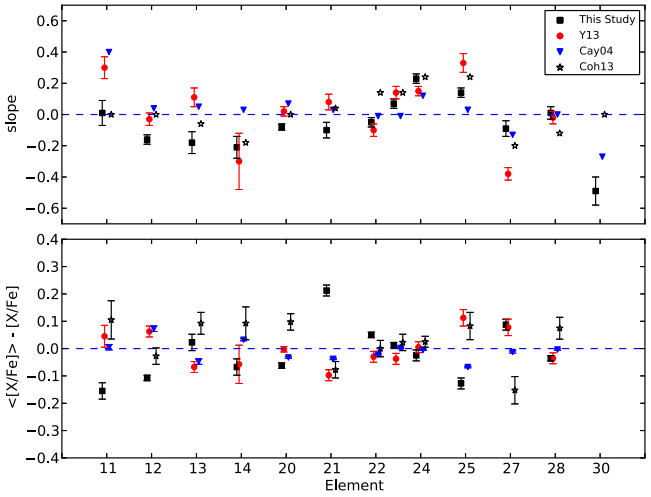

Figure 15. Top panel: the slopes of lines of best fit for each element [X/Fe]. Here, our linear regression analysis (black squares) is compared to that of Yong et al. (2013a; red circles), Cayrel et al. (2004; blue triangles), and Cohen et al. (2013; stars). For all but the last sample, errorbars on the points represent the slope uncertainties. Note that the uncertainties on the Cayrel et al. (2004) slopes are smaller than the symbols in the figure. Bottom panel: the difference between individual study mean [X/Fe] ratio for their stellar sample and the mean [X/Fe] ratio of all four studies, for elements Z = 11–30.

5. SKYMAPPER METAL-POOR STARS OF INTEREST

5.1. A New "Fe-enhanced" Metal-poor Star

One star, SMSS J034249.53–284216.0 ([Fe/H] = −2.28), has subsolar [Mg/Fe], [Ca/Fe], [Sc/Fe], [Ti I/Fe] and [Ti II/Fe] ratios, the lowest of the entire sample. In fact, it is has [X/Fe] < 0 for all elements save Si and Eu. Its S/N (mean ∼30) is less than the median value for the sample, but by no means the lowest, and the abundances for most elements are based on the measure of several lines, so these results are robust.

There is a growing number of metal-poor stars in the literature that show similar low [X/Fe] ratios (Nissen & Schuster 1997; Spite et al. 2000; Ivans et al. 2003; Cayrel et al. 2004; Honda et al. 2004; Cohen & Huang 2010; Bonifacio et al. 2011; Venn et al. 2012; Caffau et al. 2013a; Yong et al. 2013a). They have been called "α-poor" or "Fe-rich" metal-poor stars. The latter designation is likely more appropriate for those stars that show deficiencies in numerous other species in addition to the α-elements. Indeed the element abundance patterns of such stars look similar to those of more typical metal-poor stars, but shifted as a result of an additional Fe component.

Figure 16 plots the element abundance pattern of SMSS J034249.53–284216.0 (cyan squares, cyan bold line), along with other stars exhibiting low [X/Fe] ratios in the literature, relative to the mean abundances from the SkyMapper sample[15] (Table 10). We restrict the literature stars in Figure 16 to have [Fe/H] < −2, though we note that many other "Fe-enhanced" stars exist in the literature at higher metallicities (e.g., Nissen & Schuster 1997; Ivans et al. 2003; Cohen & Huang 2010; Bonifacio et al. 2011; Venn et al. 2012). As has been noted in the literature (e.g., Yong et al. 2013a), there is some scatter in the abundances of these stars. The average [X/Fe] offset from the mean SkyMapper sample abundances in Figure 16 is −0.40 dex, with a 1σ scatter of 0.16 dex (for SMSS J034249.53–284216.0, the offset is −0.52 dex). While there is scatter in the abundance patterns, the stars in general show sub-solar [X/Fe] ratios for all elements except for the Fe-peak elements Cr and Mn.

A natural explanation for the Fe-enhancements exhibited by these stars is that they formed from gas preferentially enriched with SNe Ia products rather than just SNe II (e.g., Cayrel et al. 2004; Caffau et al. 2013a; Yong et al. 2013a). Such environments exist in dwarf galaxies (indeed some known Fe-enhanced stars are in dwarf galaxies (Venn et al. 2012; Cohen & Huang 2010)), leading to the possibility that the most metal-poor of the Fe-enhanced stars in the halo originated in dwarf galaxies. That said, recent work by Kobayashi et al. (2014) has shown that the scatter and low element abundance ratios of stars in Caffau et al. (2013a) and Cohen et al. (2013) with [Fe/H] ⩽ −3 are well-matched by single core-collapse SN or hypernova yields, making a dwarf galaxy origin unnecessary. This single enrichment scenario likely does not hold for the more metal-rich stars, including SMSS J034249.53–284216.0 with [Fe/H] = −2.3. For these, the Fe enhancements may be due to variations in the progenitor masses and associated timescales of SNe Ia.

For now, these few stars (∼1%–2% of hundreds of halo stars so far subject to high-resolution spectroscopic study) indicate inhomogeneities in chemical evolution at the time of their formation, in contrast to the apparent widespread homogeneity in the bulk of metal-poor star formation (recall the small scatter and lack of correlation in [α/Fe] for the metal-poor star sample of Cayrel et al. 2004). As more such stars are found, it will be possible to investigate and better quantify the degree of inhomogeneity in star formation and chemical evolution in the early universe.

5.2. A New [Fe/H] ∼ −4 Star with High [Sr/Ba]

Although SMSS J022423.27–573705.1 first appeared in the RAVE catalog (Kordopatis et al. 2013; see Section 4.7), our work demonstrates for the first time that it is an EMP star, with [Fe/H] = −3.97 ± 0.14. With [C/Fe] = +0.07 (+0.25 after applying the Placco et al. 2014b correction), it is not one of the CEMP stars identified in Section 4.2, and its α- and Fe-peak element [X/Fe] ratios are normal (see Figures 9 and 11). However, there are no barium lines detectable in its fairly high S/N spectrum and an upper limit of [Ba/Fe] < −0.91 was obtained. In contrast, Sr lines are quite strong, giving a robust measure of [Sr/Fe] = +1.08. This [Sr/Fe] ratio is compatible with the most Sr-rich stars of comparable metallicity as seen in Roederer (2013, his Figure 2). The measured upper limit of [Eu/Fe] is +1.15 and unfortunately not helpful in further constraining the origin of the neutron-capture elements in this star. Using Equation (6) of Hansen et al. (2014a) to predict the Eu abundance from the Ba upper limit, [Eu/Fe] < +0.07.

Figure 13 shows that SMSS J022423.27–573705.1 exhibits one of largest [Sr/Ba] ratios currently known for a metal-poor star in the Milky Way halo.[16] To our knowledge, only one other star is known to have [Sr/Ba] $\gtrsim$ 2: SDSS J1422+0031, with [Fe/H] = −3.03 and [Sr/Ba] = +2.2 (Aoki et al. 2013a). Together, these two stars are the most extreme examples of the growing number of EMP stars that show large ($\gtrsim$0.8 dex) enhancements of the light neutron-capture element Sr relative

[15] These are taken to represent [X/Fe] ratios for typical halo stars with [Fe/H] < −2.5.

[16] We note that stars in the ultra-faint dwarf galaxy Segue-1 exhibit extremely low upper limits to their Sr and Ba abundances that point to intriguing neutron capture element enrichment episodes that are different from the Milky Way halo stars considered here (Frebel et al. 2014).

Table 10
Mean [X/Fe] for Different Studies

[X/Fe]	This Study			Yong et al. (2013a)			Cayrel et al. (2004)			Cohen et al. (2013)[a]		
	Mean (dex)	N	$\sigma/\sqrt{N}$ (dex)	Mean (dex)	N	$\sigma/\sqrt{N}$ (dex)	Mean (dex)	N	$\sigma/\sqrt{N}$ (dex)	Mean (dex)	N	$\sigma/\sqrt{N}$ (dex)
Na I	+0.44	83	0.03	+0.24	38	0.04	+0.28	35	0.01	+0.18	49	0.07
Mg I	+0.47	89	0.01	+0.30	60	0.02	+0.29	35	0.01	+0.39	59	0.03
Al I	−0.71	82	0.03	−0.62	54	0.02	−0.64	35	0.01	−0.78[b]	47	0.04
Si I	+0.58	71	0.03	+0.57	14	0.07	+0.48	35	0.004	+0.42	47	0.06
Ca I	+0.38	89	0.01	+0.32	60	0.01	+0.35	35	0.003	+0.22	56	0.03
Sc II	−0.11	84	0.02	+0.15	44	0.02	+0.09	35	0.003	+0.13	46	0.03
Ti I	+0.21	88	0.01	+0.29	55	0.02	+0.28	35	0.003	+0.26	59	0.03
Ti II	+0.27	88	0.01	+0.32	60	0.02	+0.28	35	0.003	+0.26	59	0.03
Cr I	−0.31	88	0.01	−0.34	54	0.02	−0.33	35	0.002	−0.36	59	0.02
Mn I	−0.42	84	0.02	−0.66	37	0.03	−0.48	35	0.003	−0.63	51	0.05
Co I	+0.12	89	0.02	+0.13	54	0.03	+0.22	35	0.004	+0.36	41	0.05
Ni I	+0.03	86	0.01	+0.03	56	0.02	−0.002	35	0.003	−0.08	42	0.04
Zn I	+0.32	30	0.04	…	…	…	+0.33	35	0.005	…	…	…

[a] These numbers were taken from Table 16 in Cohen et al. (2013) for their "Inner Halo" sample that have distances $4 < D < 15$ kpc, which more likely overlaps with the distances spanned by this SkyMapper sample.
[b] Here we have removed the 0.6 dex NLTE correction Cohen et al. (2013) applied to their Al abundances in order to compare them to the LTE abundances of the other studies.

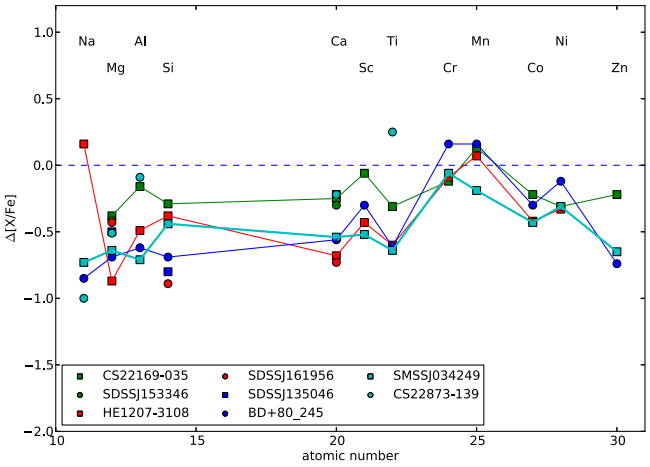

Figure 16. Abundance difference, in the sense ([X/Fe]−[X/Fe]$_{\rm Ref}$) for "Fe-enhanced" stars relative to that of the mean [X/Fe] ratios found in our study (Table 10). The star in this study, SMSS J034249.53–284216.0, is indicated by cyan squares and cyan bold line. For simplicity, lines connecting individual element abundances are only drawn for stars where most of the species have been measured; some stars in this figure only have [α/Fe] reported in the literature. The patterns for all the stars are generally similar. References for the literature sample include: Spite et al. (2000), Ivans et al. (2003), Cayrel et al. (2004), Bonifacio et al. (2011), Caffau et al. (2013a), and Yong et al. (2013a).

to the heavier neutron-capture element Ba, as have been found in several studies (e.g., Honda et al. 2004; Aoki et al. 2005, 2013a; Lai et al. 2008; Hollek et al. 2011; Cohen et al. 2013; Placco et al. 2014a). Such stars are generally taken as evidence for an extra neutron-capture element production mechanism in addition to the main r-process as the source of the heaviest elements in the early universe (e.g., Travaglio et al. 2004; Honda et al. 2006; Sneden et al. 2008; Jacobson & Frebel 2014). Mechanisms such as the Light Element Primary Process (LEPP; Travaglio et al. 2004), the weak r-process (Ishimaru et al. 2005), the weak s-process (Heil et al. 2009), and the truncated r-process (Boyd et al. 2012) have been invoked to explain the existence of stars with large enhancements of Sr, Y, and Zr relative to Ba and Eu.

We inspected the spectrum of SMSS J022423.27–573705.1 for the presence of other neutron-capture species absorption lines, and were able to detect several Y and Zr lines, but no lines of species belonging to the second peak (e.g., Ba, La, Ce, Nd) or higher. Spectrum synthesis of four Y II and three Zr II lines resulted in [Y/Fe] = +0.80 ± 0.26 and [Zr/Fe] = +1.06 ± 0.16 (s.d.). SMSS J022423.27–573705.1 is therefore strongly enhanced in the first peak neutron-capture species, with no detectable presence of heavier species.

Figure 17 shows the abundance pattern of SMSS J022423.27–573705.1 relative to that of HD 122563, the poster star exhibiting such light neutron-capture element enhancements with [Sr/Ba] = +0.76 (Honda et al. 2006). To minimize any systematics in this comparison, we have carried out our own abundance analysis of HD 122563, the results of which are presented in Table 11. (We refer the reader to Frebel et al. (2013) for details regarding the data, but note that the analysis presented here is separate from the results in that work.) These two stars show similar abundance patterns for most elements save for Sr, Y, and Zr. It is clear from this Figure that whatever the source(s) is (are) that produced this pattern of heavy elements (i.e., the LEPP (Travaglio et al. 2004)), it (they) operated even more strongly in the enrichment that led to the formation of SMSS J022423.27–573705.1 than for HD 122563.

Rapidly rotating, low metallicity massive stars ("spinstars") have been considered a possible source of light neutron-capture elements in the early universe, and models of such have been able to reproduce the s-process element enhancements of low-metallicity field stars and globular cluster stars (e.g., Pignatari et al. 2008; Chiappini et al. 2011; Frischknecht et al. 2012).[17] The abundance pattern produced by the 25 $M_{\odot}$, [Fe/H] = −3.8 model of Frischknecht et al. (2012) agrees relatively well with that of SMSS J022423.27–573705.1 (Figure 17) for the elements in common (Co, Ni, Sr; see their Figure 1). They

[17] See, however, the results of Ness et al. (2014) which do not support the spinstar origin scenario in the case of globular cluster NGC 6522 (Chiappini et al. 2011).

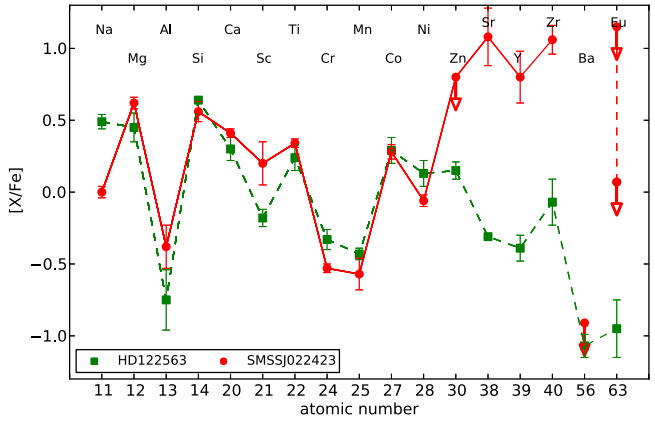

Figure 17. LTE element abundance pattern for star SMSS J022423.27–573705.1 relative to that of HD 122563 (abundances given in Table 11). Note that the abundance patterns are quite similar for most elements, save for the neutron capture species. The large [X/Fe] ratios for Sr, Y, and Zr in SMSS J022423.27–573705.1 are most striking, while its Ba abundance is just an upper limit. Two upper limits are indicated for [Eu/Fe], connected by a dashed line: +1.15 and +0.07, as measured in the spectrum and as predicted using the relation of Hansen et al. (2014a), respectively.

Table 11
Element Abundances of HD 122563

Species	logϵ(X)	# lines	s.d.	[X/H]	[X/Fe]
C I	5.53	2	0.04	−3.20	−0.43
Na I	3.96	2	0.05	−2.28	+0.49
Mg I	5.28	7	0.10	−2.32	+0.45
Al I	2.93	2	0.21	−3.52	−0.60
Si I	5.38	2	0.01	−2.13	+0.64
Ca I	3.87	22	0.08	−2.47	+0.30
Sc II	0.20	5	0.06	−2.91	−0.14
Ti I	2.29	30	0.07	−2.66	+0.11
Ti II	2.42	46	0.09	−2.53	+0.24
Cr I	2.54	19	0.07	−3.10	−0.33
Cr II	2.88	3	0.09	−2.76	+0.01
Mn I	2.23	7	0.04	−3.20	−0.43
Fe I	4.73	193	0.12	−2.77	⋯
Fe II	4.75	27	0.11	−2.75	⋯
Co I	2.51	5	0.09	−2.48	+0.29
Ni I	3.58	18	0.09	−2.64	+0.13
Zn I	1.94	2	0.06	−2.62	+0.14
Sr II	−0.21	2	0.01	−3.08	−0.31
Y II	−0.95	5	0.06	−3.16	−0.39
Zr II	−0.26	4	0.10	−2.84	−0.07
Ba II	−1.66	2	0.08	−3.84	−1.07
Eu II	−3.20	1	⋯	−3.72	−0.95

do not give production factors for the elements Cr and Mn, which are both low in our star. Their model also predicts a yield of Zn relatively larger than Co and Ni, but we could not detect Zn lines in the spectrum of SMSS J022423.27–573705.1. Of the three stars in our sample with [Fe/H] < −3.5, only one star has a detectable Zn line in its spectrum. An upper limit EW measure for the Zn I λ4810 in the spectrum of SMSS J022423.27–573705.1 corresponds to [Zn/Fe] < +0.8, which, together with the other element abundances, is consistent with the pattern from Frischknecht et al. (2012).

It is not straightforward to compare the abundances of elements below the Fe-peak (Mn and lower) to the models of Frischknecht et al. (2012), because these models do not include element production in the supernova explosion itself (R. Hirschi, 2014, private communication). As more of these stars are found, and the abundances of larger numbers of neutron-capture elements are measured in them, it will be easier to disentangle the presence of different production mechanisms and to identify their production sites.

6. SUMMARY AND CONCLUSIONS

We have presented a detailed chemical element abundance analysis of the first SkyMapper metal-poor star candidates that were observed at high spectroscopic resolution. Based on a 1D LTE element abundance analysis, the stellar parameters and element abundances for these stars show them to be bona fide metal-poor halo stars, as indicated by how well they match the abundance patterns of halo stars in the literature.

The main finding of this study is the verification of EMP star candidates selected based on photometry from the SkyMapper Southern Sky Survey and medium-resolution spectroscopy. Excluding previously known EMP stars in our sample, we have confirmed 38 new stars to have [Fe/H] < −3.0, 8 of which have [Fe/H] < −3.5. More importantly, the EMP candidate selection technique based on the SkyMapper photometry has been improved over the course of this program, and indeed the most iron-poor star known to date (with [Fe/H] < −7; Keller et al. 2014), was confirmed by its high-resolution Magellan-MIKE spectrum during the accumulation of the sample presented here.

Concerning the abundances of particular elements or of particular stars in the study presented here, we have found the following:

1. Eight stars previously known in the literature have been recovered by the SkyMapper survey, six of which were previously known to be EMPs. We find reasonable to excellent agreement with the results of other studies for four of these objects: $T_{\rm eff}$ within 250 K; [Fe/H] within 0.4 dex. One star, which was not previously identified as metal-poor, turns out to be the most metal-poor star in our sample, with [Fe/H] = −3.97.
2. After correcting stellar C abundances for evolutionary effects, 24 stars are classified as CEMP stars based on the criterion of Aoki et al. (2007). Considering only stars with [Fe/H] $\leqslant$ −3, this results in a CEMP fraction of 39%, in good agreement with other studies. Seven stars have [C/Fe] > 1 and are classified as CEMP-no stars. Of these, five have [Fe/H] < −3.
3. Our most metal-poor star with [Fe/H] = −3.97, has [Sr/Ba] $\gtrsim$ 2, showing an extreme ratio of light to heavy neutron-capture element abundances. This indicates that the weak r-process (or other mechanism) can yield more extreme light neutron-capture element enhancements than previously thought.
4. One star with [X/Fe] $\leqslant$ 0 for all elements save Si and Eu, is likely a member of the growing population of "Fe-enhanced" metal-poor stars in the literature.
5. Four stars have r-process enhancements [Eu/Fe] > 1 and are classified as r-II stars, while another 22 appear to be at least mildly r-process enhanced based on their [Eu/Fe] ratios. The relative fractions of r-I (22/122 = 18%) and r-II stars (4/122 = 3%) are comparable to those found by Barklem et al. (2005) (>14% and 3%, respectively). We caution, however, that the metallicity ranges of the two

samples are different (Barklem et al. 2005 had no stars with $[Fe/H] < -3.5$), so the similarity of the r-I/II fractions may be coincidental.

These results successfully demonstrate the capability of the SkyMapper survey to find more stars at the very metal-poor end of the Milky Way halo MDF, as well as stars exhibiting interesting abundance signatures. The increased sample size of these metal-poor stars will improve our understanding of chemical enrichment in the early epochs of the universe, as well as reveal insight into the nature of the Pop III stars that were the first seeds of chemical enrichment.

This research has made use of the SIMBAD database, operated at CDS, Strasbourg, France and of NASA's Astrophysics Data System Bibliographic Services. This publication also makes use of data products from the Two Micron All Sky Survey, which is a joint project of the University of Massachusetts and the Infrared Processing and Analysis Center/California Institute of Technology, funded by the National Aeronautics and Space Administration and the National Science Foundation. We thank the referee for helpful suggestions that improved the presentation of this work. R. Hirschi is thanked for informative discussions regarding the models of Frischknecht et al. (2012). A.F. acknowledges support from NSF grant AST-1255160. A.C. was partially supported by the European Union FP7 programme through ERC grant 320360. M.S.B, G.D.C., and S.K. acknowledge support from the Australian Research Council through Discovery Projects grant DP12010137. M.A. has been supported by an Australian Research Council Laureate fellowship (grant FL110100012). K.L. acknowledges the European Union FP7-PEOPLE-2012-IEF grant No. 328098. B.P.S. has been supported by an Australian Research Council Laureate fellowship (grant FL0992131). The work of J.M.P. and Q.Y. was supported by the MIT UROP program and J.M.W. was supported by the Research Science Institute at MIT. Australian access to the Magellan Telescopes was supported through the Collaborative Research Infrastructure Strategy of the Australian Federal Government.

REFERENCES

Abel, T., Bryan, G. L., & Norman, M. L. 2002, Sci, 295, 93
Andrievsky, S. M., Spite, F., Korotin, S. A., et al. 2011, A&A, 530, A105
Andrievsky, S. M., Spite, M., Korotin, S. A., et al. 2009, A&A, 494, 1083
Aoki, W., Beers, T. C., Christlieb, N., et al. 2007, ApJ, 655, 492
Aoki, W., Beers, T. C., Lee, Y. S., et al. 2013a, AJ, 145, 13
Aoki, W., Beers, T. C., Sivarani, T., et al. 2008, ApJ, 678, 1351
Aoki, W., Honda, S., Beers, T. C., et al. 2005, ApJ, 632, 611
Aoki, W., Norris, J. E., Ryan, S. G., Beers, T. C., & Ando, H. 2002, ApJL, 576, L141
Aoki, W., Suda, T., Boyd, R. N., Kajino, T., & Famiano, M. A. 2013b, ApJL, 766, L13
Asplund, M. 2005, ARA&A, 43, 481
Asplund, M., Grevesse, N., Sauval, A. J., & Scott, P. 2009, ARA&A, 47, 481
Barklem, P. S., Christlieb, N., Beers, T. C., et al. 2005, A&A, 439, 129
Baumueller, D., & Gehren, T. 1997, A&A, 325, 1088
Beers, T. C., Preston, G. W., & Shectman, S. A. 1992, AJ, 103, 1987
Bergemann, M. 2011, MNRAS, 413, 2184
Bergemann, M., & Gehren, T. 2008, A&A, 492, 823
Bergemann, M., Hansen, C. J., Bautista, M., & Ruchti, G. 2012a, A&A, 546, A90
Bergemann, M., Lind, K., Collet, R., Magic, Z., & Asplund, M. 2012b, MNRAS, 427, 27
Bernstein, R., Shectman, S. A., Gunnels, S. M., Mochnacki, S., & Athey, A. E. 2003, Proc. SPIE, 4841, 1694
Bessell, M., Bloxham, G., Schmidt, B., et al. 2011, PASP, 123, 789
Bonifacio, P., Caffau, E., François, P., et al. 2011, AN, 332, 251
Bonifacio, P., Sbordone, L., Caffau, E., et al. 2012, A&A, 542, A87
Boyd, R. N., Famiano, M. A., Meyer, B. S., et al. 2012, ApJL, 744, L14
Bromm, V., & Larson, R. B. 2004, ARA&A, 42, 79
Caffau, E., Bonifacio, P., François, P., et al. 2011, Natur, 477, 67
Caffau, E., Bonifacio, P., François, P., et al. 2013a, A&A, 560, A15
Caffau, E., Bonifacio, P., Sbordone, L., et al. 2013b, A&A, 560, A71
Carney, B. W., Laird, J. B., Latham, D. W., & Aguilar, L. A. 1996, AJ, 112, 668
Casey, A. R. 2014, arXiv:1405.5968
Castelli, F., & Kurucz, R. L. 2004, arXiv:astro-ph/0405087
Cayrel, R., Depagne, E., Spite, M., et al. 2004, A&A, 416, 1117
Chiappini, C., Frischknecht, U., Meynet, G., et al. 2011, Natur, 472, 454
Christlieb, N., Bessell, M. S., Beers, T. C., et al. 2002, Natur, 419, 904
Christlieb, N., Schörck, T., Frebel, A., et al. 2008, A&A, 484, 721
Cohen, J. G., Christlieb, N., McWilliam, A., et al. 2004, ApJ, 612, 1107
Cohen, J. G., Christlieb, N., Thompson, I., et al. 2013, ApJ, 778, 56
Cohen, J. G., & Huang, W. 2010, ApJ, 719, 931
Cui, X.-Q., Zhao, Y.-H., Chu, Y.-Q., et al. 2012, RAA, 12, 1197
François, P., Depagne, E., Hill, V., et al. 2003, A&A, 403, 1105
Frebel, A. 2010, AN, 331, 474
Frebel, A., Aoki, W., Christlieb, N., et al. 2005, Natur, 434, 871
Frebel, A., Casey, A. R., Jacobson, H. R., & Yu, Q. 2013, ApJ, 769, 57
Frebel, A., Christlieb, N., Norris, J. E., et al. 2006, ApJ, 652, 1585
Frebel, A., & Norris, J. E. 2015, ARA&A, in press, arXiv:1501.06921
Frebel, A., Simon, J. D., & Kirby, E. N. 2014, ApJ, 786, 74
Frischknecht, U., Hirschi, R., & Thielemann, F.-K. 2012, A&A, 538, L2
Gehren, T., Liang, Y. C., Shi, J. R., Zhang, H. W., & Zhao, G. 2004, A&A, 413, 1045
Gustafsson, B., Edvardsson, B., Eriksson, K., et al. 2008, A&A, 486, 951
Hansen, C. J., Montes, F., & Arcones, A. 2014a, ApJ, 797, 123
Hansen, T., Hansen, C. J., Christlieb, N., et al. 2014b, ApJ, 787, 162
Hartwick, F. D. A. 1976, ApJ, 209, 418
Heil, M., Juseviciute, A., Käppeler, F., et al. 2009, PASA, 26, 243
Hirano, S., Hosokawa, T., Yoshida, N., et al. 2014, ApJ, 781, 60
Hobbs, L. M., Thorburn, J. A., & Rebull, L. M. 1999, ApJ, 523, 797
Hollek, J. K., Frebel, A., Roederer, I. U., et al. 2011, ApJ, 742, 54
Honda, S., Aoki, W., Ishimaru, Y., Wanajo, S., & Ryan, S. G. 2006, ApJ, 643, 1180
Honda, S., Aoki, W., Kajino, T., et al. 2004, ApJ, 607, 474
Howes, L. M., Asplund, M., Casey, A. R., et al. 2014, MNRAS, 445, 4241
Ishimaru, Y., Wanajo, S., Aoki, W., Ryan, S. G., & Prantzos, N. 2005, NuPhA, 758, 603
Ivans, I. I., Sneden, C., James, C. R., et al. 2003, ApJ, 592, 906
Jacobson, H. R., & Frebel, A. 2014, JPhG, 41, 044001
Johnson, J. A. 2002, ApJS, 139, 219
Keller, S. C., Bessell, M. S., Frebel, A., et al. 2014, Natur, 506, 463
Keller, S. C., Schmidt, B. P., Bessell, M. S., et al. 2007, PASA, 24, 1
Kelson, D. D. 2003, PASP, 115, 688
Kim, Y.-C., Demarque, P., Yi, S. K., & Alexander, D. R. 2002, ApJS, 143, 499
Kobayashi, C., Ishigaki, M. N., Tominaga, N., & Nomoto, K. 2014, ApJL, 785, L5
Kobayashi, C., Umeda, H., Nomoto, K., Tominaga, N., & Ohkubo, T. 2006, ApJ, 653, 1145
Kordopatis, G., Gilmore, G., Steinmetz, M., et al. 2013, AJ, 146, 134
Kurucz, R., & Bell, B. 1995, Atomic Line Data, Kurucz CD-ROM No. 23 (Cambridge, MA: Smithsonian Astrophysical Observatory)
Lai, D. K., Bolte, M., Johnson, J. A., et al. 2008, ApJ, 681, 1524
Lawler, J. E., & Dakin, J. T. 1989, JOSAB, 6, 1457
Lawler, J. E., Guzman, A., Wood, M. P., Sneden, C., & Cowan, J. J. 2013, ApJS, 205, 11
Li, H. N., Christlieb, N., Schörck, T., et al. 2010, A&A, 521, A10
Li, H.-N., Zhao, G., Christlieb, N., et al. 2015, ApJ, 798, 110
Lind, K., Asplund, M., & Barklem, P. S. 2009, A&A, 503, 541
Lind, K., Asplund, M., Barklem, P. S., & Belyaev, A. K. 2011, A&A, 528, A103
Lind, K., Bergemann, M., & Asplund, M. 2012, MNRAS, 427, 50
Liske, J., Lemon, D. J., Driver, S. P., Cross, N. J. G., & Couch, W. J. 2003, MNRAS, 344, 307
Mashonkina, L. 2013, A&A, 550, A28
Mashonkina, L., Gehren, T., Travaglio, C., & Borkova, T. 2003, A&A, 397, 275
Mashonkina, L., Korn, A. J., & Przybilla, N. 2007, A&A, 461, 261
McWilliam, A., Preston, G. W., Sneden, C., & Searle, L. 1995, AJ, 109, 2757

Ness, M., Asplund, M., & Casey, A. R. 2014, MNRAS, 445, 2994
Nissen, P. E., & Schuster, W. J. 1997, A&A, 326, 751
Norris, J. E., Bessell, M. S., Yong, D., et al. 2013, ApJ, 762, 25
Norris, J. E., Christlieb, N., Korn, A. J., et al. 2007, ApJ, 670, 774
Norris, J. E., Ryan, S. G., & Beers, T. C. 1996, ApJS, 107, 391
Norris, J. E., Ryan, S. G., & Beers, T. C. 1999, ApJS, 123, 639
Pietrinferni, A., Cassisi, S., Salaris, M., & Castelli, F. 2006, ApJ, 642, 797
Pignatari, M., Gallino, R., Meynet, G., et al. 2008, ApJL, 687, L95
Placco, V. M., Frebel, A., Beers, T. C., et al. 2013, ApJ, 770, 104
Placco, V. M., Frebel, A., Beers, T. C., et al. 2014a, ApJ, 781, 40
Placco, V. M., Frebel, A., Beers, T. C., & Stancliffe, R. J. 2014b, ApJ, 797, 21
Placco, V. M., Kennedy, C. R., Beers, T. C., et al. 2011, AJ, 142, 188
Roederer, I. U. 2013, AJ, 145, 26
Roederer, I. U., Cowan, J. J., Karakas, A. I., et al. 2010a, ApJ, 724, 975
Roederer, I. U., Cowan, J. J., Preston, G. W., et al. 2014a, MNRAS, 445, 2970
Roederer, I. U., Preston, G. W., Thompson, I. B., et al. 2014b, AJ, 147, 136
Roederer, I. U., Sneden, C., Thompson, I. B., Preston, G. W., & Shectman, S. A. 2010b, ApJ, 711, 573
Ruchti, G. R., Bergemann, M., Serenelli, A., Casagrande, L., & Lind, K. 2013, MNRAS, 429, 126
Ryan, S. G., & Norris, J. E. 1991, AJ, 101, 1835
Ryan, S. G., Norris, J. E., & Beers, T. C. 1996, ApJ, 471, 254
Schlaufman, K. C., & Casey, A. R. 2014, ApJ, 797, 13
Schörck, T., Christlieb, N., & Cohen, J. G. 2009, A&A, 507, 817
Skrutskie, M. F., Cutri, R. M., & Stiening, R. 2006, AJ, 131, 1163
Sneden, C. A. 1973, PhD thesis, Univ. Texas
Sneden, C., Cowan, J. J., & Gallino, R. 2008, ARA&A, 46, 241
Sobeck, J. S., Kraft, R. P., Sneden, C., et al. 2011, AJ, 141, 175
Spite, M., Cayrel, R., Plez, B., et al. 2005, A&A, 430, 655
Spite, M., Depagne, E., Nordström, B., et al. 2000, A&A, 360, 1077
Spite, M., & Spite, F. 2014, AN, 335, 65
Stacy, A., & Bromm, V. 2014, ApJ, 785, 73
Starkenburg, E., Hill, V., Tolstoy, E., et al. 2010, A&A, 513, A34
Susa, H., Hasegawa, K., & Tominaga, N. 2014, ApJ, 792, 32
Travaglio, C., Gallino, R., Arnone, E., et al. 2004, ApJ, 601, 864
Venn, K. A., Shetrone, M. D., Irwin, M. J., et al. 2012, ApJ, 751, 102
Wood, M. P., Lawler, J. E., Sneden, C., & Cowan, J. J. 2013, ApJS, 208, 27
Yanny, B., Rockosi, C., Newberg, H. J., et al. 2009, AJ, 137, 4377
Yong, D., Norris, J. E., Bessell, M. S., et al. 2013a, ApJ, 762, 26
Yong, D., Norris, J. E., Bessell, M. S., et al. 2013b, ApJ, 762, 27
York, D. G., Adelman, J., Anderson, J. E., Jr., et al. 2000, AJ, 120, 1579
Zhao, G., Chen, Y.-Q., Shi, J.-R., et al. 2006, ChJAA, 6, 265